https://doi.org/10.5194/egusphere-2026-1038
Preprint. Discussion started: 9 March 2026
© Author(s) 2026. CC BY 4.0 License.

Long-term Study of Gravity Wave Potential Energy and OH Airglow Emissions from 22 years of TIMED/SABER Observations

Toyese Tunde Ayorinde[1], Cristiano Max Wrasse[1], Luiz Fillip Rodrigues Vital[2,3], Anderson Vestena Bilibio[4], Gabriel Augusto Giongo[1], Hisao Takahashi[1], and Cosme Alexandre Oliveira Barros Figueiredo[4]

[1]Space Weather Division, National Institute for Space Research (INPE), São José dos Campos, SP, Brazil
[2]State Key Laboratory of Space Weather, National Space Science Center of the Chinese Academy of Sciences (NSSC/CAS), Beijing, China
[3]State University of Paraíba (UEPB), Campina Grande, Brazil
[4]Unidade Acadêmica de Física, Universidade Federal de Campina Grande, Campina Grande, PB, Brazil

Correspondence: Toyese Tunde Ayorinde (toyese.ayorinde@inpe.br)

Abstract. Using 22 years (2002-2023) of TIMED/SABER satellite observations, we investigate the long-term coupling between mesospheric hydroxyl (OH) airglow and gravity wave potential energy (Ep). Continuous wavelet transform analysis extracts gravity wave signatures from temperature perturbations, and multiple linear regression decomposes the observed variability into contributions from solar activity, geomagnetic activity, the Quasi-Biennial Oscillation (QBO), and El Niño–Southern Oscillation (ENSO). Three major findings emerge. First, OH emissions and gravity wave Ep are positively coupled, with statistically significant ($p < 0.05$) correlation coefficients of 0.3–0.7 that peak during winter at mid-latitudes. Second, long-term trends reveal contrasting latitudinal patterns: OH trends are negative at mid-latitudes in both hemispheres (-1 to $-5 \times 10^{-10}\,\mathrm{W\,m^{-3}\,yr^{-1}}$), consistent with mesospheric cooling, whereas Ep trends are positive at mid-latitudes (up to $5.3 \times 10^{-2}\,\mathrm{J\,kg^{-1}\,yr^{-1}}$), exceeding current model predictions. Both quantities show weaker trends near the equator. Third, a novel decomposition methodology separates temperature-driven chemical responses from non-thermal dynamical effects, revealing that solar forcing operates primarily through thermal mechanisms and accounts for 10–15 % of OH variance, while QBO and ENSO influence mesospheric chemistry through dynamical pathways. ENSO drives negative OH responses yet enhances Ep, and QBO responses exhibit equatorial–midlatitude dipole patterns. Semi-annual oscillations dominate equatorial variability, while annual oscillations prevail at Southern Hemisphere mid-latitudes.

1 Introduction

The mesosphere and lower thermosphere (MLT), extending from approximately 50 to 110 km altitude, represents an interface between the neutral lower atmosphere and the plasma-dominated environment of space (Beig et al., 2003; Mlynczak, 1997). This region serves as a critical coupling zone where the gravity wave energy and momentum from the lower atmosphere are deposited, influencing global atmospheric circulation, thermal balance, and chemical composition (Fritts and Alexander, 2003; Alexander et al., 2010). Understanding the long-term evolution of mesospheric processes is relevant for predicting atmospheric responses to climate change, as the mesosphere exhibits sensitivity to greenhouse gas increases through radiative

https://doi.org/10.5194/egusphere-2026-1038
Preprint. Discussion started: 9 March 2026
© Author(s) 2026. CC BY 4.0 License.

cooling mechanisms—with model studies predicting cooling rates of approximately 1–3 K per decade in the upper mesosphere (Beig et al., 2003; Laštovička et al., 2006; Akmaev et al., 2006).

The primary agents of vertical coupling are internal atmospheric gravity waves, buoyancy-driven oscillations generated in the troposphere by orographic forcing, deep convection, and jet stream instabilities (Fritts and Alexander, 2003; Sato et al., 2009). As these waves propagate vertically into the rarefied middle atmosphere, their amplitudes grow exponentially, eventually leading to instability, breaking, and momentum deposition that drives large-scale circulation patterns (Baldwin et al., 2001; Alexander et al., 2010).

Gravity wave potential energy (Ep) quantifies the energy available for momentum deposition and atmospheric mixing, providing a direct measure of wave activity in the middle atmosphere (Fritts and Alexander, 2003). The hydroxyl (OH) airglow, a chemiluminescent emission originating from a layer centered at approximately 87 km altitude, results from the exothermic reaction $H + O_3 \rightarrow OH^* + O_2$, where the asterisk denotes a vibrationally excited state (Mlynczak, 1997; Smith et al., 2013). The airglow's brightness and rotational temperature are sensitive to local atmospheric conditions, making it a tracer for both chemical processes and gravity wave activity (Li et al., 2011; Xu et al., 2012; Taylor et al., 2009). Volume emission rate (VER) measurements provide direct quantification of OH emission intensity suitable for long-term trend analysis (Sivakandan et al., 2016). The coupling between gravity waves and OH emissions operates through two mechanisms: thermal, where wave-induced temperature perturbations modulate reaction rates, and dynamical, where waves vertically advect reactant species (particularly atomic oxygen and ozone) (Li et al., 2011; Tarasick and Shepherd, 1992; Nielsen et al., 2009).

Ground-based studies using all-sky imagers and spectrometers have characterized gravity wave properties through airglow signatures, revealing seasonal variations and regional differences in wave activity (Taylor et al., 2009; Ejiri et al., 2003; Tang et al., 2014). Satellite observations from TIMED/SABER, operational since 2002, have enabled global climatologies of both gravity wave activity and OH emissions (Zhang et al., 2012; Ern et al., 2011; Gao et al., 2010). SABER studies have characterized seasonal and QBO variations in OH emissions—for example, Gao et al. (2010) found QBO-related OH variations of approximately 2–4% at tropical latitudes—as well as responses to sudden stratospheric warmings (Gao et al., 2011), solar cycle effects (Fytterer et al., 2015), and hydroxyl emission mechanisms (Xu et al., 2012).

Gravity wave climatologies have revealed latitudinal and seasonal patterns in wave activity and momentum flux (Zhang et al., 2012; Ern et al., 2011). Long-term trend studies have identified mesospheric cooling associated with increasing greenhouse gas concentrations (Beig et al., 2003; Offermann et al., 2010; Zhao et al., 2020). Recent investigations have employed empirical orthogonal function (EOF) analysis—a statistical technique that identifies the dominant spatial patterns of variability in a dataset—to characterize gravity wave variability patterns and their relationships with tropospheric forcing (Ayorinde et al., 2024), examined stratospheric gravity wave potential energy and its connections to tropospheric parameters (Ayorinde et al., 2023), and investigated the modulation of tropical stratospheric gravity wave activity by climate variability modes (Ayorinde et al., 2025).

Despite this progress, the nature and variability of the long-term, global relationship between gravity wave Ep and OH emissions remain poorly understood. Previous studies have been limited in temporal coverage, with most analyses spanning less than a decade, or in scope, focusing on either gravity waves or OH chemistry but not their coupled behavior (Gao et al.,

https://doi.org/10.5194/egusphere-2026-1038
Preprint. Discussion started: 9 March 2026
© Author(s) 2026. CC BY 4.0 License.

2010; Fytterer et al., 2015; Zhang et al., 2012; Ern et al., 2011). Key open questions remain: How do solar variability, QBO, and ENSO drive chemistry-dynamics coupling, and how do these drivers modulate the OH-Ep coupling itself? The relative contributions of thermal versus non-thermal processes to OH variability under different forcing conditions have not been quantified. Investigating long-term trends in gravity wave activity and their relationship to chemical changes could be essential for constraining climate model predictions of mesospheric evolution.

The primary objectives of this work are to characterize the long-term variability and trends of mesospheric OH airglow and gravity wave Ep using 22 years of TIMED/SABER observations, quantify the statistical relationships between OH emissions and gravity wave activity across different latitudes and seasons, assess the responses of both quantities to external forcing mechanisms including solar variability, QBO, and ENSO, decompose OH variability into temperature-driven and non-thermal dynamical components to identify the dominant physical mechanisms, and provide observational constraints for atmospheric models to improve representations of chemistry-dynamics coupling in the mesosphere. This 22-year dataset provides insights not apparent from shorter-term studies, including the ability to separate solar cycle effects from long-term trends and to characterize the full range of ENSO and QBO variability.

This paper is structured as follows: Section 2 details the TIMED/SABER dataset and methodology. Section 3 presents results including latitudinal profiles of trends and forcing responses, seasonal oscillations, and correlation analyses. Section 4 discusses the physical implications of the findings, including the decomposition analysis. Section 5 presents conclusions.

2 Methodology

2.1 TIMED/SABER Instrument and Data

This study utilizes observations from the Sounding of the Atmosphere using Broadband Emission Radiometry (SABER) instrument aboard the Thermosphere Ionosphere Mesosphere Energetics and Dynamics (TIMED) satellite (Russell III et al., 1999; Mlynczak, 1997). The SABER instrument is a 10-channel broadband limb-scanning infrared radiometer that measures atmospheric emissions in the 1.27 to 17 µm spectral range, providing vertical profiles of kinetic temperature, geopotential height, and volume emission rates (VER, in units of $\mathrm{W\,m^{-3}}$ or photons $\mathrm{cm^{-3}\,s^{-1}}$) of various atmospheric constituents from approximately 10 to 120 km altitude (Mlynczak et al., 2005; Russell III et al., 1999). SABER employs a limb-scanning technique, viewing the Earth's atmosphere tangentially through the limb scanning to obtain vertical profiles with high vertical resolution (approximately 2 km). The instrument scans the limb from the surface to approximately 400 km altitude, with a horizontal sampling resolution of about 400 km along the satellite track. The TIMED satellite operates in a 625 km circular orbit with a 74° inclination, providing near-global coverage from 83°S to 83°N latitude, with the latitudinal coverage varying seasonally due to the satellite's yaw cycle (Russell III et al., 1999). A known limitation of SABER is the inability to observe both polar regions simultaneously due to the yaw maneuver cycle, which restricts continuous high-latitude coverage.

This orbital configuration enables SABER to sample each latitude and local time approximately every 60 days, providing temporal and spatial coverage for climatological studies. For this investigation, we used SABER Level 2A version 2.0 data products spanning from January 2002 to December 2023, encompassing over two decades of continuous observations. The

https://doi.org/10.5194/egusphere-2026-1038
Preprint. Discussion started: 9 March 2026
© Author(s) 2026. CC BY 4.0 License.

primary data products employed include: (1) kinetic temperature profiles derived from CO_2 15 µm limb emission measurements, with an estimated precision of 1-2 K in the mesosphere (Remsberg et al., 2008); (2) OH_{VER} derived from the 1.6 and 2.0 µm OH Meinel band emissions, providing information about the OH airglow layer structure and intensity (Mlynczak et al., 2005); and (3) geopotential height profiles that enable accurate altitude registration of the measurements. The SABER temperature measurements are suited for gravity wave studies due to their high vertical resolution and global coverage. SABER's temperature sensitivity of 1- 2 K enables detection of gravity wave signatures in the middle atmosphere (Ern et al., 2011; Zhang et al., 2012). Similarly, the OH_{VER} measurements provide information about the mesospheric airglow layer, which serves as a tracer for atmospheric dynamics and chemistry (Xu et al., 2012; Gao et al., 2010). The long-term stability and consistency of SABER measurements have been validated through comparisons with other satellite instruments and ground-based observations, confirming their suitability for climatological trend analysis (Remsberg et al., 2008; Garcia et al., 2014).

2.2 OH Airglow Data Processing and Peak Identification

The hydroxyl (OH) airglow layer in the mesosphere represents a tracer for atmospheric dynamics and chemistry, originating from the exothermic reaction between atomic hydrogen and ozone: $H + O_3 \rightarrow OH^* + O_2$, where OH^* denotes vibrationally excited hydroxyl (Mlynczak, 1997). The resulting vibrationally excited OH molecules emit characteristic infrared radiation in the Meinel band system, which SABER detects at 1.6 and 2.0 µm wavelengths (Mlynczak et al., 2005). This study focuses on the peak of the OH emission layer, following established methodologies that have demonstrated the peak region's sensitivity to atmospheric perturbations and its reduced susceptibility to retrieval uncertainties compared to integrated column measurements (Offermann et al., 2010; Sivakandan et al., 2016).

The OH_{VER} profiles are processed through a multi-step quality control and analysis procedure. First, individual profiles are screened for data quality using the SABER data quality flags, removing profiles with instrument anomalies, cloud contamination, or retrieval convergence issues. Profiles with unrealistic VER values (negative emissions or values exceeding 1×10^{-6} W m^{-3}) is excluded from the analysis (Xu et al., 2012). We apply altitude registration corrections using co-measured geopotential heights to ensure consistent altitude referencing. The identification of the OH emission peak follows the methodology established by Gu et al. (2024) for characterizing the OH emission layer. The OH peak identification algorithm employs a multi-step quality control approach: (1) smooth the VER profile using a 3-point running mean to reduce noise, (2) identify the altitude of maximum VER within the expected mesospheric range (75–95 km), (3) ensure that the identified peak represents a genuine OH emission maximum by requiring the peak value to exceed half of the profile maximum, and (4) verify the peak structure by checking that the VER decreases monotonically on both sides of the identified maximum (Gu et al., 2024). Profiles where the peak cannot be unambiguously identified or where multiple peaks of similar magnitude exist are flagged and excluded from further analysis; approximately 5–10% of profiles are discarded through this quality control procedure. The peak identification algorithm extracts two key parameters for each profile: (1) the peak OH_{VER} intensity (W m^{-3}), representing the maximum emission rate, and (2) the peak altitude (km), indicating the height of maximum emission.

The VER provides a direct measure of OH emission intensity that is suitable for long-term trend analysis and comparison with atmospheric models (Sivakandan et al., 2016). Following peak identification, the data undergo temporal and spatial bin-

https://doi.org/10.5194/egusphere-2026-1038
Preprint. Discussion started: 9 March 2026
© Author(s) 2026. CC BY 4.0 License.

ning to create regular time series suitable for climatological analysis. Individual profiles are aggregated into monthly means within 10° latitude bins, extending from 50°S to 50°N. This binning strategy balances the need for adequate statistical sampling with sufficient spatial resolution to capture latitudinal variations in OH behavior. Only latitude bins containing at least 20 individual profiles per month are retained to ensure statistical robustness (Gao et al., 2010).

2.3 Gravity Wave Ep Estimation

Gravity wave Ep per unit mass (E_p) represents a measure of wave activity and provides direct quantification of the energy available for momentum deposition and atmospheric mixing (Fritts and Alexander, 2003). The calculation of gravity wave potential energy (Ep) from SABER temperature measurements follows established methodologies that have been extensively validated in previous studies (Ern et al., 2011; Zhang et al., 2012; Liu et al., 2017; Ayorinde et al., 2023, 2024, 2025). The approach involves extracting gravity wave temperature perturbations from the background atmospheric state and converting these perturbations to Ep using the relationship between wave-induced temperature fluctuations and vertical displacement of air parcels. Following the methodology detailed in Ayorinde et al. (2023) for stratospheric gravity wave potential energy estimation and extended by Ayorinde et al. (2024) for long-term variation analysis, the processing begins with the extraction of temperature perturbations from SABER kinetic temperature profiles. Background temperature profiles are obtained by removing large-scale planetary and Kelvin wave signatures by following the approach detailed by Ayorinde et al. (2024) and Ayorinde et al. (2025).

Temperature perturbations are calculated as $T'(z) = T(z) - \bar{T}(z)$, where $T(z)$ is the observed temperature profile and $\bar{T}(z)$ is the background temperature obtained from the running mean filter. Additional filtering is applied to isolate gravity wave activities, with the temperature perturbations undergoing vertical wavelength filtering to retain perturbations with vertical wavelengths between 3 and 20 km. This wavelength range is chosen to capture gravity waves reliably detected by SABER's vertical resolution while excluding short-scale instrumental noise (wavelengths $<$ 3 km) and planetary wave signals (wavelengths $>$ 20 km) (Liu et al., 2017; Ayorinde et al., 2023). Temperature perturbations are isolated using continuous wavelet transform (CWT) with a Morlet wavelet, providing superior time-frequency localization for gravity wave characterization as described by Ayorinde et al. (2024). The Ep per unit mass is calculated using the fundamental relationship (Fritts and Alexander, 2003):

$$E_p = \frac{1}{2}\left(\frac{g}{N}\right)^2 \left(\frac{T'}{T_0}\right)^2 \tag{1}$$

where g is the gravitational acceleration (9.81 m s^{-2}), N is the buoyancy frequency (Brunt-Väisälä frequency), T' is the gravity wave temperature perturbation amplitude, and T_0 is the background temperature. The buoyancy frequency is calculated from the background temperature profile using:

$$N^2 = \frac{g}{T_0}\left(\frac{dT_0}{dz} + \frac{g}{c_p}\right) \tag{2}$$

where dT_0/dz is the background temperature gradient, z is altitude, and c_p is the specific heat of air at constant pressure (approximately 1004 J kg^{-1} K^{-1}). The Ep calculations are performed within 5-km-thick altitude layers centered on the OH peak altitude. This layer thickness was chosen to provide a representative measure of gravity wave activity in the immediate vicinity of the OH layer while maintaining sufficient vertical resolution to capture altitude-dependent variations and ensuring

https://doi.org/10.5194/egusphere-2026-1038
Preprint. Discussion started: 9 March 2026
© Author(s) 2026. CC BY 4.0 License.

adequate statistical sampling of wave perturbations. The temperature perturbation amplitude T' is calculated as the root-mean-square (RMS) value of the filtered perturbations within each altitude layer, following the statistical approach validated by Ayorinde et al. (2023) for stratospheric gravity wave analysis.

Quality control procedures ensure the reliability of Ep estimates. Profiles with unrealistic buoyancy frequencies ($N^2 < 0$, indicating convective instability, or $N^2 > 1 \times 10^{-3}\ s^{-2}$, exceeding physically plausible values for the mesosphere) are excluded, and Ep values exceeding 1000 $J\,kg^{-1}$ are flagged as outliers. The final Ep dataset undergoes the same spatial and temporal binning procedure as the OH data, creating monthly mean time series in 10° latitude bins for climatological analysis.

2.4 Long-term Trend Analysis and Multiple Linear Regression

This study employs a multiple linear regression (MLR) approach, following the methodology previously used by Zhao et al. (2020) and widely used in middle atmospheric trend studies (Beig et al., 2003; Offermann et al., 2010). The MLR framework quantifies contributions from specific physical drivers while isolating the long-term trend. While the F10.7 index is not a perfect proxy for solar EUV radiation, it remains the most widely used and validated proxy for long-term atmospheric studies due to its continuous record and strong correlation with solar EUV emissions (Lean, 2018). The MLR analysis begins with the construction of time series representing primary sources of atmospheric variability. Solar activity is represented by using the 10.7 cm solar radio flux (F10.7 index), obtained from the National Research Council of Canada, which serves as a proxy for solar ultraviolet radiation that drives mesospheric photochemistry (Lean, 2018). The F10.7 index is suited for atmospheric studies because it correlates with solar EUV emissions that control photochemical processes in the mesosphere and lower thermosphere (Zhao et al., 2020).

Solar Flux Processing and Estimation

The daily F10.7 solar radio flux index and Kp index (3-hourly) spanning from 2002 to 2019 serve as proxies for solar extreme ultraviolet (EUV) radiation and geomagnetic activity, respectively. The F10.7 flux index is frequently utilized in studies examining solar activity, particularly in the context of middle and upper atmospheric trends (Yuan et al., 2019). The mean F10.7 is computed as

$$\mathrm{F10.7} = \frac{\mathrm{F10.7_{adj}} + \mathrm{F10.7_{ctr81}}}{2}, \tag{3}$$

where $\mathrm{F10.7_{adj}}$ represents the 10.7 cm solar radio flux, adjusted for Earth's orbital radius, and expressed in units of $10^{-22}\ \mathrm{W/m^2/Hz}$. The term $\mathrm{F10.7_{ctr81}}$ denotes the 81-day arithmetic mean of the daily adjusted F10.7 values, centered on the specific day in question. This method of averaging F10.7 is considered effective for capturing variations in solar activity (Richards et al., 1994). Both F10.7 and Kp indices were retrieved from the Celestrak website (http://celestrak.com/SpaceData/). Geomagnetic activity is represented by the planetary K-index (Kp), obtained from the GFZ German Research Centre for Geosciences, which quantifies global geomagnetic disturbances that can influence the upper atmosphere through energetic particle precipitation (Matzka et al., 2021).

https://doi.org/10.5194/egusphere-2026-1038
Preprint. Discussion started: 9 March 2026
© Author(s) 2026. CC BY 4.0 License.

The daily F10.7 values undergo a multi-step processing procedure to extract the solar cycle while removing short-term variability. The first step involves application of an 81-day centering running mean filter to the raw daily F10.7 data:

$$\overline{F_{10.7}}(t) = \frac{1}{81}\sum_{i=-40}^{40} F_{10.7}(t+i) \tag{4}$$

where $\overline{F_{10.7}}(t)$ is the smoothed solar flux at time t, and $F_{10.7}(t+i)$ represents the daily values within the 81-day window centered on day t. The 81-day window was chosen because it effectively removes solar rotation effects (27-day periodicity, with three complete rotations captured) and short-term solar variability while preserving the 11-year solar cycle variations that are most relevant for mesospheric chemistry and dynamics (Zhao et al., 2020). This window length is standard in middle atmospheric studies and provides a balance between noise reduction and temporal resolution. Following the temporal smoothing, the F10.7 time series is normalized to facilitate interpretation of the regression coefficients and enable comparison across different studies. The normalization is performed using:

$$F_{10.7}^{norm}(t) = \frac{\overline{F_{10.7}}(t) - \langle\overline{F_{10.7}}\rangle}{\sigma_{\overline{F_{10.7}}}} \tag{5}$$

Where $\langle\overline{F_{10.7}}\rangle$ is the long-term mean of the smoothed F10.7 over the entire analysis period (2002-2023), and $\sigma_{\overline{F_{10.7}}}$ is the corresponding standard deviation. This normalization ensures that the regression coefficients represent the atmospheric response per standard deviation change in solar activity, facilitating physical interpretation and comparison with other forcing mechanisms. To account for potential nonlinear atmospheric responses to solar forcing, both linear and quadratic terms of the normalized F10.7 are included in the MLR model. The quadratic term is calculated as:

$$F_{10.7}^{quad}(t) = [F_{10.7}^{norm}(t)]^2 - \langle[F_{10.7}^{norm}]^2\rangle \tag{6}$$

where the subtraction of the mean squared value ensures that the quadratic term is orthogonal to the linear term, preventing multicollinearity issues in the regression analysis (Zhao et al., 2020). The correlation coefficient between the linear and quadratic terms over the study period is less than 0.05, confirming their near-orthogonality. This orthogonalization is essential for obtaining stable and interpretable regression coefficients, particularly important for photochemical processes that may exhibit threshold behaviors or saturation effects at high solar activity levels.

The processed F10.7 time series undergoes additional quality control to maintain consistency over the multi-decade analysis period. Data gaps shorter than 5 days are filled using linear interpolation, while longer gaps are handled through spectral interpolation based on the dominant solar cycle periodicity. The final F10.7 dataset provides a representation of solar variability suitable for investigating solar-atmospheric coupling in the mesosphere and lower thermosphere. The QBO is represented using monthly mean zonal wind data at 30 mb and 50 mb pressure levels from the Free University of Berlin QBO database (Newman et al., 2016). The ENSO is characterized using the Multivariate ENSO Index (MEI) from the NOAA Physical Sciences Laboratory, which combines multiple oceanic and atmospheric variables to provide a measure of ENSO state (Wolter and Timlin, 1998). We note that solar activity and geomagnetic activity are often correlated; however, the inclusion of both in the MLR model allows for separation of their distinct effects, with the Kp index capturing short-term geomagnetic disturbances not represented by the smoothed F10.7 index. Before MLR analysis, both the dependent variables (OH_{VER} and Ep) and the independent

https://doi.org/10.5194/egusphere-2026-1038
Preprint. Discussion started: 9 March 2026
© Author(s) 2026. CC BY 4.0 License.

proxy variables undergo deseasonalization to remove the dominant annual and semi-annual cycles. This is accomplished by fitting and subtracting harmonic functions of the form:

$$S(t) = \sum_{n=1}^{3} [A_n \cos(n\omega t) + B_n \sin(n\omega t)] \tag{7}$$

where $\omega = 2\pi/365.25$ days^{-1}, and A_n and B_n are the amplitude coefficients for the n-th harmonic (Zhao et al., 2020). The choice of three harmonics (annual, semi-annual, and ter-annual) was based on spectral analysis of the data, which showed that these three components capture >95% of the seasonal variance. This approach effectively removes the seasonal cycles while preserving inter-annual variability and long-term trends. The MLR model is formulated as:

$$\begin{aligned} Y(t) = {} & C_0 + C_1 \cdot t + C_2 \cdot F_{10.7}(t) + C_3 \cdot F_{10.7}(t) + C_4 \cdot QBO_{30}(t) \\ & + C_5 \cdot QBO_{50}(t) + C_6 \cdot MEI(t) + C_7 \cdot Kp(t) + \epsilon(t) \end{aligned} \tag{8}$$

where $Y(t)$ represents the deseasonalized time series of either OH_{VER} or Ep, t is time in years, C_0 is the intercept, C_1 is the linear trend coefficient representing secular change per year, C_2 and C_3 are the linear and quadratic solar response coefficients respectively, C_4 and C_5 are the QBO response coefficients at 30 mb and 50 mb, C_6 is the ENSO response coefficient, C_7 is the geomagnetic activity response coefficient, and $\epsilon(t)$ is the error term (Zhao et al., 2020). The inclusion of both linear and quadratic terms for the solar flux accounts for potential nonlinear responses to solar variability (Lean, 2018).

The MLR analysis is performed separately for each 10° latitude bin and for different seasonal subsets (annual mean, DJF months, and JJA months) to investigate latitudinal and seasonal dependencies in the responses. Statistical significance of the regression coefficients is assessed using Student's t-test, with p-values reported throughout; coefficients with $p < 0.05$ are considered statistically significant. The overall model performance is evaluated using the coefficient of determination (R^2) and the root-mean-square error (RMSE). Uncertainty estimates for the trend coefficients are derived from the covariance matrix of the regression coefficients, which accounts for the interdependence of the predictors and temporal autocorrelation in the residuals (Weatherhead et al., 1998). Trend robustness is evaluated via sensitivity tests that vary the analysis period, proxy variables, and deseasonalization approach. Residual analysis identifies any systematic patterns suggesting missing forcings or model deficiencies.

Figure 1 presents the time series of key atmospheric indices used in the MLR analysis. The solar flux (F10.7) exhibits the characteristic 11-year solar cycle with maxima around 2002-2003 and 2014-2015, and a minimum around 2007-2010. The Multivariate ENSO Index (MEI) captures El Niño-Southern Oscillation variability, with El Niño events in 2009-2010, 2015-2016, and 2023, while La Niña conditions dominate during 2007-2008, 2010-2012, and 2017-2018. The QBO at 30 mb shows alternating easterly and westerly wind phases with an average period of approximately 28 months.

https://doi.org/10.5194/egusphere-2026-1038
Preprint. Discussion started: 9 March 2026
© Author(s) 2026. CC BY 4.0 License.

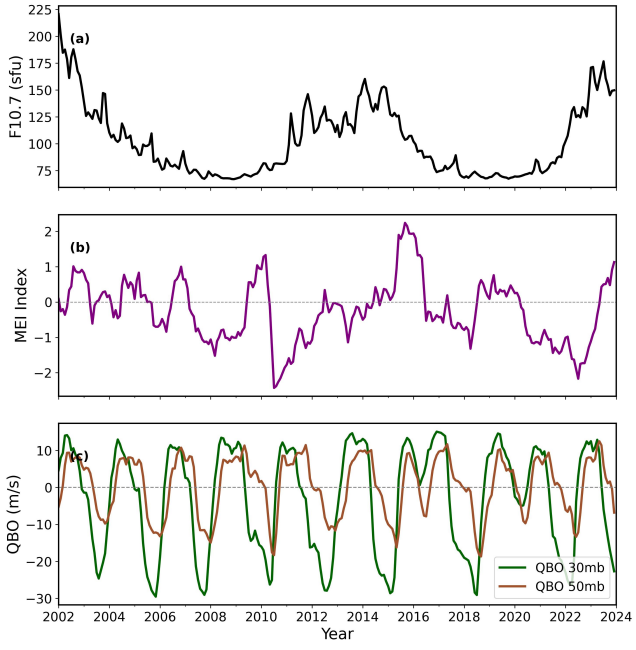

Figure 1. Time series of solar and geophysical indices from January 2002 to December 2023, used as explanatory variables. **(a)** The monthly mean solar radio flux at 10.7 cm (F10.7) in solar flux units (sfu), which serves as a proxy for solar activity, clearly showing solar cycles 23 and 24. **(b)** The bimonthly Multivariate El Niño-Southern Oscillation (ENSO) Index (MEI), where positive values correspond to El Niño phases and negative values to La Niña phases. **(c)** The monthly mean zonal winds representing the Quasi-Biennial Oscillation (QBO) at two pressure levels in the tropics: 30 mb (dark green line) and 50 mb (sienna line). Negative (positive) values indicate easterly (westerly) wind regimes.

3 Results

3.1 Latitudinal and Temporal Evolution OH and Ep

Figure 2 reveals the temporal evolution of mesospheric OH airglow and gravity wave activity over the 22-year SABER observation. The top panel shows the OH_{VER}, which exhibits latitudinal and seasonal patterns consistent with the underlying photochemical processes governing OH production and loss in the mesosphere. The OH_{VER} displays seasonal variations with maximum values occurring during local December-January-February (DJF) and June-July-August (JJA) months at mid-latitudes, reaching peak emission rates of approximately 8–10 $\times$ 10^{-7} W m^{-3} in both hemispheres. This seasonal pattern likely reflects the coupling between atomic hydrogen and ozone concentrations, both of which are modulated by seasonal changes in atmospheric dynamics and photochemistry (Xu et al., 2012; Gao et al., 2010). The latitudinal structure of OH_{VER} shows an asymmetry between hemispheres, with higher emission rates observed in the Northern Hemisphere (NH), particularly during DJF months. This hemispheric asymmetry can be attributed to differences in planetary wave activity and stratosphere-mesosphere coupling, which affect the transport of atomic oxygen and hydrogen species that control OH chemistry (Smith et al., 2013; Gao et al.,

https://doi.org/10.5194/egusphere-2026-1038
Preprint. Discussion started: 9 March 2026
© Author(s) 2026. CC BY 4.0 License.

2011). The equatorial region exhibits relatively stable OH emission rates throughout the year, with values typically ranging between 4–6 $\times$ 10^{-7} W m^{-3}, consistent with the reduced seasonal variability expected in tropical latitudes where solar zenith angle variations are minimal.

The middle panel displays the Ep at the OH maximum altitude, providing characterization of gravity wave activity in the mesosphere. The Ep exhibits temporal and spatial variability, with values ranging from less than 36 J/kg to over 48 J/kg. Features include increased gravity wave activity during JJA months at mid-latitudes, consistent with tropospheric wave generation and propagation conditions during these periods (Ern et al., 2011; Zhang et al., 2012). This seasonal pattern is consistent with findings from Ayorinde et al. (2024), who demonstrated that gravity wave Ep over South America shows seasonal dependence, with maximum values during austral JJA months when tropospheric forcing is largest. The spatial distribution of gravity wave activity shows hemispheric asymmetries, with higher Ep values in the NH, caused by different topographic forcing and convective storm activity (Anderson et al., 2021).

The equatorial region shows higher Ep values but with inter-annual variability, likely associated with the QBO and other tropical atmospheric phenomena (Ern et al., 2017). The solar cycle modulation is visible in both OH_{VER} and Ep throughout the observation period. The solar maximum around 2014–2015 corresponds to increased OH concentrations globally, reflecting the increased production of atomic hydrogen through solar Lyman-α radiation (Mlynczak et al., 2013). Ep exhibits latitude-dependent solar cycle variations, indicating that solar forcing modulates gravity waves through multiple pathways: altered atmospheric stability and background winds (Liu et al., 2017). The bottom panel shows the altitude of the OH maximum, which varies between approximately 75 and 90 km with latitudinal and temporal patterns. The OH peak altitude exhibits a seasonal cycle, with higher altitudes during local DJF months in the NH and JJA months in the Southern Hemisphere (SH), consistent with seasonal changes in atmospheric temperature structure and the vertical distribution of atomic oxygen (Marsh et al., 2006).

https://doi.org/10.5194/egusphere-2026-1038
Preprint. Discussion started: 9 March 2026
© Author(s) 2026. CC BY 4.0 License.

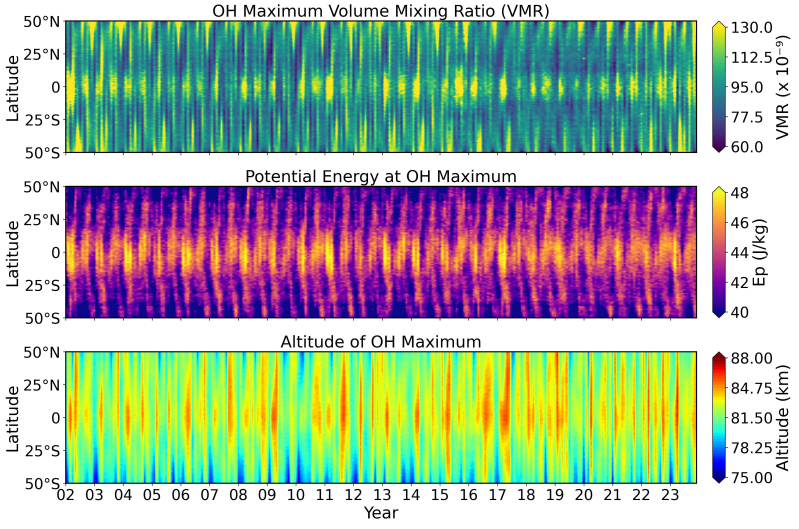

Figure 2. Temporal evolution (2002-2023) of zonally averaged parameters as a function of latitude. (Top) OH Maximum Volume Emission Rate (VER). (Middle) Ep at OH Maximum (Ep). (Bottom) Altitude of OH_{VER} Maximum.

3.2 Seasonal Cycles of OH and Ep

Figure 3 shows the seasonal decomposition analysis, providing characterization of the annual variations and the residual inter-annual variability. The seasonal cycles reveal the annual rhythms that characterize mesospheric variability. For OH_{VER}, the mid-latitude stations ($50°$N and $50°$S) show DJF and JJA maxima, reaching peak values of 4-5 $\times$ 10^{-7} μm at mid-latitudes. The tropical station ($10°$N) exhibits smaller seasonal variations. The Ep seasonal cycles show larger amplitudes, particularly at mid-latitudes, where DJF and JJA values can exceed their opposite seasons by factors of 2-3, with maxima reaching 7-15 J/kg. This reflects the seasonal dependence of gravity wave generation in the troposphere, with increased wave activity during these months when storm tracks are most active. The NH shows higher Ep values compared to the SH, particularly during DJF months, reflecting orographic and convective wave sources. The residual time series (Figure 3b) reveals inter-annual variability that remains after removing the seasonal patterns, showing evidence for solar cycle modulation, ENSO influences, and long-term trends. The OH_{VER} residuals show variations with evidence of solar cycle modulation, while the Ep residuals exhibit higher frequency variability with larger amplitude fluctuations.

OH_{VER} seasonal cycles show strong latitudinal and hemispheric variations. At $50°$ latitude, both hemispheres exhibit maxima during local winter (DJF in NH, JJA in SH) with amplitudes of 0.4-0.5 $\times$ 10^{-7} μm, driven by solar zenith angle and atmospheric dynamics. The seasonal amplitude decreases equatorward: $/sim$0.2-0.3 $\times$ 10^{-7} μm at $30°$ (NH winter maximum) and minimal variation at $10°$ with near-symmetric hemispheric behavior. The Ep seasonal cycles display larger relative amplitudes, with mid-latitude ($50°$) maxima of 7-15 J/kg which is 3-4 times the seasonal minima. Residual variability reveals inter-annual fluctuations including enhanced OH_{VER} during the 2014-2015 solar maximum and persistent hemispheric asymmetries throughout the observation period.

https://doi.org/10.5194/egusphere-2026-1038
Preprint. Discussion started: 9 March 2026
© Author(s) 2026. CC BY 4.0 License.

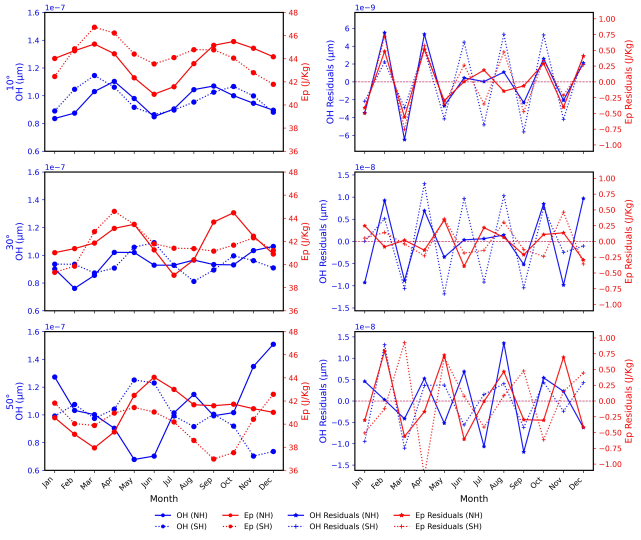

Figure 3. Mean seasonal cycles and residuals at different latitudes. (a) Mean seasonal cycle of OH_{VER} (left y-axis) and Ep (right y-axis) at 10°, 30°, and 60° latitude. The top panel corresponds to 10°latitude, the middle panel to 30°latitude, and the bottom panel to 60°latitude. Solid lines represent the Northern Hemisphere (NH) and dotted lines represent the Southern Hemisphere (SH). Blue lines correspond to OH, while red lines correspond to Ep. The figure shows distinct seasonal patterns with December-January-February (DJF) and June-July-August (JJA) representing the primary seasonal contrasts in each hemisphere. (b) Corresponding residuals from the mean seasonal cycle for each time series, revealing inter-annual variability and long-term trends after removing the dominant seasonal activities.

3.3 Latitudinal Profiles of Trends and Solar Responses

The linear trend analysis (Figure 4) shows latitudinal patterns in the long-term evolution of both OH_{VER} and Ep over the 22-year observation period. Statistical significance of the trends is indicated by blue stars ($p < 0.05$) and red stars ($p \geq 0.05$) overlaying the profiles, as detailed in the figure caption. For OH_{VER} (Figure 4a-b), the annual trends show negative values at mid-latitudes in both hemispheres (25°–50°) and weaker trends (closer to zero) in tropical regions (±15°). The magnitude of the OH trends ranges from -0.2 to +0.4 $\times$ 10^{-9} μm per year. Seasonal decomposition reveals distinct DJF and JJA trend patterns. JJA trends are predominantly positive across all latitudes, particularly in NH subtropics. DJF trends show hemispheric asymmetry: positive in the SH, variable in the NH.

Ep trends (Figure 4c–d) differ from OH_{VER}, exhibiting stronger latitudinal gradients and larger relative amplitudes. Mid-latitudes show positive trends in both hemispheres, while equatorial regions display weak or negative trends. Near the equator (±15°), the trends in potential energy (E_p) are weak and statistically insignificant, remaining close to zero. In contrast, significant positive trends emerge in the mid-latitudes of both hemispheres (25° to 50°).

In the NH, the E_p trend strengthens from approximately 0.03 J kg^{-1} yr^{-1} at 25°N to a peak of about 0.05 J kg^{-1} yr^{-1} between 30°N and 40°N, before decreasing to around 0.04 J kg^{-1} yr^{-1} at 50°N. A similar pattern is observed in the SH, where the trend peaks at approximately 0.05 J kg^{-1} yr^{-1} around 40°S. A seasonal analysis reveals distinct patterns. During

https://doi.org/10.5194/egusphere-2026-1038
Preprint. Discussion started: 9 March 2026
© Author(s) 2026. CC BY 4.0 License.

June-July-August (JJA), trends are consistently positive across all latitudes. However, during December-January-February (DJF), the patterns show hemispheric asymmetry. The NH mid-latitudes exhibit strong positive trends, reaching up to $8-10$ J kg^{-1} yr^{-1}, whereas the SH trends are smaller and more variable.

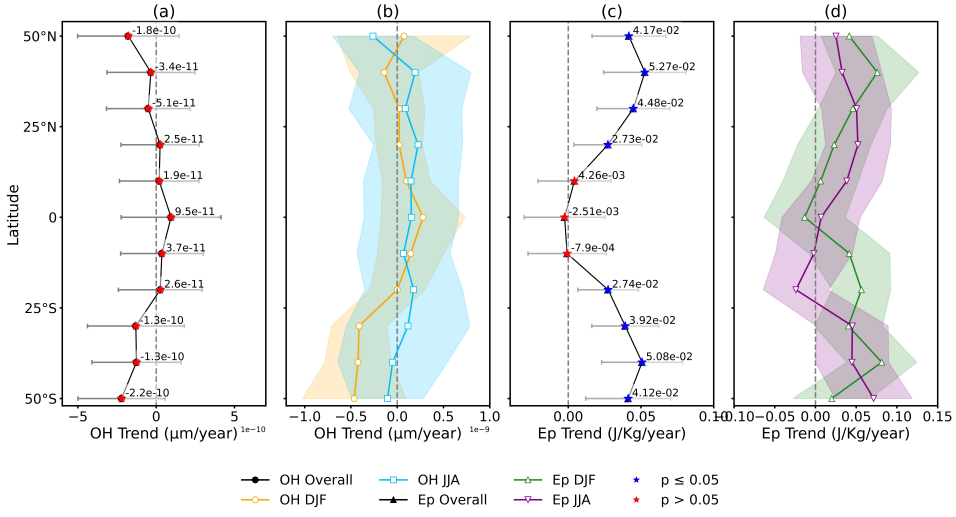

Figure 4. Latitudinal profiles of the linear trend. (a) Overall annual trend for OH_{VER}. (b) Seasonal trend for OH_{VER} during JJA (orange) and DJF (cyan). (c) Overall annual trend for Ep. (d) Seasonal trend for Ep during JJA (green) and DJF (purple). Error bars in (a, c) and shaded areas in (b, d) indicate the 95% confidence interval of the trend coefficients. The blue stars overlaying the overall profile indicate statistically significant values ($p < 0.05$), while red stars indicate values that are not statistically significant ($p \geq 0.05$).

The solar response analysis (Figure 5) shows the relationship between solar variability and mesospheric processes across all latitudes. As with the trend analysis, statistical significance is indicated by blue and red stars overlaying the profiles (see figure caption for details). For OH_{VER} (Figure 5a-b), the solar response is positive across all latitudes with an equatorial maximum reaching values of 0.8-1.0 $\times$ 10^{-7} μm per 100 sfu (solar flux units). JJA responses are larger than DJF responses, particularly in the NH. The hemispheric asymmetries in solar response are present during DJF months, with the SH showing larger responses than the NH. The Ep solar response (Figure 5c-d) shows patterns with both positive and negative responses depending on latitude and season. The annual response shows positive values in tropical regions and negative values at mid-latitudes. The seasonal decomposition of Ep solar response shows differences between JJA and DJF patterns. JJA responses are positive across most latitudes, while DJF responses show hemispheric asymmetries with positive responses in the SH and negative responses in the NH at mid-latitudes.

https://doi.org/10.5194/egusphere-2026-1038
Preprint. Discussion started: 9 March 2026
© Author(s) 2026. CC BY 4.0 License.

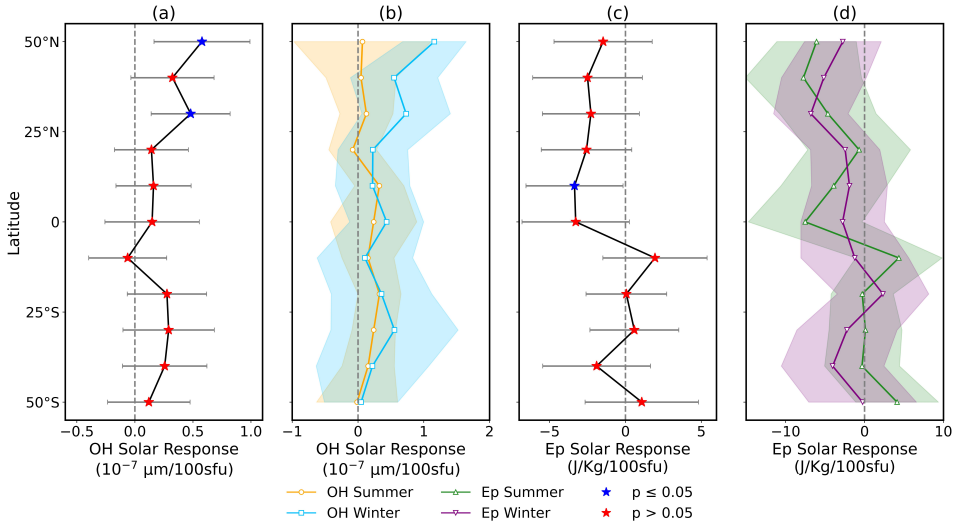

Figure 5. Latitudinal profiles of the solar response. (a) Overall annual response for OH_{VER}. (b) Seasonal response for OH_{VER} during JJA (orange) and DJF (cyan). (c) Overall annual response for Ep. (d) Seasonal response for Ep during JJA (green) and DJF (purple). Error bars in (a, c) and shaded areas in (b, d) indicate the 95% confidence interval of the regression coefficients. The blue stars overlaying the overall profile indicate statistically significant values ($p < 0.05$), while red stars indicate values that are not statistically significant ($p \geq 0.05$).

The hemispheric asymmetries in solar responses (Figure 5) show contrasting behavior between OH and Ep. For OH (Figure 5a-b), both hemispheres show positive solar responses, with the SH exhibiting larger responses at mid-latitudes during DJF months. The Ep solar responses (Figure 5c-d) show hemispheric differences during the DJF months. The SH displays positive solar responses at most latitudes, while the NH shows negative solar responses at mid-latitudes during DJF.

3.4 Quasi-Biennial Oscillation and ENSO Responses

Figures 6 and 7 examine the responses of mesospheric OH and gravity wave activity to two primary modes of tropical atmospheric variability: the QBO and the ENSO. The QBO response analysis (Figure 6) reveals patterns of mesospheric coupling to stratospheric wind oscillations. Statistical significance of the responses is indicated by blue stars ($p < 0.05$) and red stars ($p \geq 0.05$) overlaying the overall profiles, as shown in the figure captions.

The OH response to the QBO in Figure 6a shows a dipole between the equator and midlatitudes. Around the equator ($\pm 15°$), QBO30 produces positive responses ($+2.8 \times 10^{-9}$ μm/(m s^{-1})), while QBO50 induces negative values near -1.0×10^{-9} μm/(m s^{-1}). In contrast, both hemispheres at 25°–50° show weaker and opposite-signed trends: in the NH, QBO30 responses are negative (-0.3 to -0.8×10^{-9} μm/(m s^{-1})) while QBO50 yields positive ($+0.2$ to $+0.9 \times 10^{-9}$ μm/(m s^{-1})). The SH shows a similar pattern, with QBO30 negative (-0.9 to -1.4×10^{-9} μm/(m s^{-1})) and QBO50 positive ($\sim +0.9$ to $+1.1 \times 10^{-9}$ μm/(m s^{-1})). Thus, equatorial OH is modulated with opposite phase between QBO30 and QBO50, while midlatitudes show a smaller but consistent opposing trend. Around the equator, variability is evident, with QBO30 responses shifting between positive and

https://doi.org/10.5194/egusphere-2026-1038
Preprint. Discussion started: 9 March 2026
© Author(s) 2026. CC BY 4.0 License.

negative depending on season, particularly during JJA. In the NH midlatitudes, QBO50 trends dominate as positive anomalies, whereas in the SH midlatitudes, both QBO30 and QBO50 yield small but oppositely signed contributions, with seasonality introducing scatter. Overall, the seasonal structure indicates that the equatorial trend is the largest and most sensitive to phase, while midlatitudes remain weaker and seasonally modulated.

Ep responses (Figure 6c) to the QBO also show equatorial–midlatitude contrasts. At the equator ($\pm 15°$), Ep regressions are mixed, with QBO30 alternating between slightly negative (-0.11 to -0.08 J kg^{-1}/(m s^{-1})) and positive ($+0.06$ to $+0.09$ J kg^{-1}/(m s^{-1})), while QBO50 remains near zero to slightly negative (-0.07 to -0.20 J kg^{-1}/(m s^{-1})). In the NH 25°–50°N, Ep responses to QBO30 are positive, peaking around $+0.25$ J kg^{-1}/(m s^{-1}), while QBO50 trends slightly negative (-0.01 to -0.20 J kg^{-1}/(m s^{-1})). In the SH midlatitudes, QBO30 is positive ($+0.05$ to $+0.09$ J kg^{-1}/(m s^{-1})), with QBO50 negative (-0.1 to -0.2 J kg^{-1}/(m s^{-1})). This indicates that Ep is modulated by the QBO in the NH midlatitudes, particularly by QBO30.

Figure 6d shows strong seasonal and latitudinal dependence in QBO modulation. Equatorial Ep remains near-zero or negative year-round, whereas NH mid-latitudes display seasonally dependent responses: positive under QBO30 during JJA, negative or weak under QBO50. In the SH midlatitudes, Ep responses are less consistent but show positive anomalies under QBO30, especially during JJA, and negative or near-zero under QBO50. Seasonality thus enhances the midlatitude asymmetry, with NH responses larger and more coherent than SH.

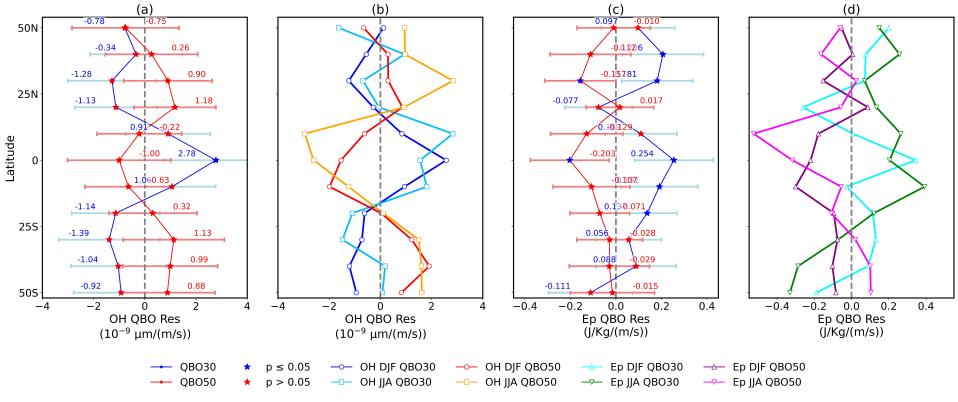

Figure 6. Latitudinal profiles of the QBO response for OH_{VER} and Ep. (a, c) The overall annual response to QBO at 30 mb and 50 mb for OH_{VER} and Ep, respectively. (b, d) The seasonal (JJA and DJF) response to QBO at 30 mb and 50 mb for OH_{VER} and Ep, respectively. Different colors and markers correspond to the specific proxy and season as detailed in the legend. Error bars indicate the 95% confidence interval of the coefficients. The blue stars overlaying the overall profile indicate statistically significant values ($p < 0.05$), while red stars indicate values that are not statistically significant ($p \geq 0.05$).

The ENSO response analysis (Figure 7) shows ENSO responses of OH and Ep across latitude bands. As indicated by the blue and red stars in the figure, statistical significance varies with latitude (see figure caption for details). Figure 7a indicates that OH ENSO responses are negative across all latitudes, with the largest values in the SH (-3.72×10^{-7} μm/MEI at 50°S,

https://doi.org/10.5194/egusphere-2026-1038
Preprint. Discussion started: 9 March 2026
© Author(s) 2026. CC BY 4.0 License.

-2.67×10^{-7} μm/MEI at 35°S) and smaller values in the NH (-2.15×10^{-7} μm/MEI at 25°N, weakening to -0.18×10^{-7} μm/MEI at 50°N). Around the equatorial region (±15°), OH decreases are present (-2.11×10^{-7} μm/MEI at the equator, -2.12×10^{-7} μm/MEI at 15°S). Figure 7b separates seasonal signals, showing that both DJF (orange) and JJA (blue) responses are negative throughout, with larger negative anomalies during JJA, especially in the tropics and subtropics, while DJF shows weaker responses. Figure 7c depicts Ep ENSO response, which is positive across latitudes. Near the equator (±15°), the response is small (0.03–0.04 J kg^{-1}/MEI), increasing toward higher latitudes: 0.21 J kg^{-1}/MEI at 50°N and 0.17 J kg^{-1}/MEI at 50°S. Figure 7d shows the seasonal breakdown of Ep responses: both DJF (green) and JJA (purple) display positive anomalies across most latitudes, with larger responses in JJA, particularly in the equatorial and SH regions, whereas DJF is more moderate.

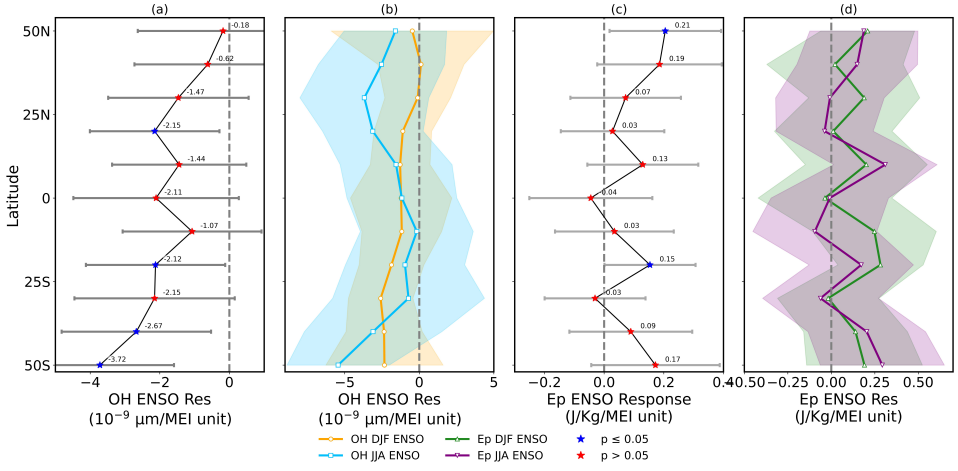

Figure 7. Latitudinal profiles of the ENSO response. (a) Overall annual response for OH_{VER}. (b) Seasonal response for OH_{VER} during JJA (orange) and DJF (cyan). (c) Overall annual response for Ep. (d) Seasonal response for Ep during JJA (green) and DJF (purple). Error bars in (a, c) and shaded areas in (b, d) indicate the 95% confidence interval of the regression coefficients. The blue stars overlaying the overall profile indicate statistically significant values ($p < 0.05$), while red stars indicate values that are not statistically significant ($p \geq 0.05$).

3.5 Correlation Analysis and Index Relationships

Figure 8 provides the analysis of the correlation patterns between deseasonalized and detrended OH_{VER} and Ep time series and various atmospheric indices. The correlation analysis for OH_{VER} (Figure 8c) shows positive correlations across all latitudes with maximum values of 0.6-0.7 in tropical regions. The ENSO correlations show a latitudinal structure with maximum values in tropical and subtropical regions, reaching correlations of 0.3-0.4. The QBO correlations are weaker, with the 30 mb index exhibiting larger correlations than the 50 mb index in most regions. The Ep correlations (Figure 8d) show different patterns compared to OH_{VER}. The solar correlations are weaker and more variable, with both positive and negative values depending on latitude. The ENSO and QBO correlations for Ep show latitudinal variations with larger correlations in tropical and sub-

https://doi.org/10.5194/egusphere-2026-1038
Preprint. Discussion started: 9 March 2026
© Author(s) 2026. CC BY 4.0 License.

tropical regions. The QBO correlations show differences between the 30 mb and 50 mb indices. The ENSO correlations show hemispheric asymmetries, with larger correlations in the NH.

The variance decomposition analysis (Figure 8) shows the percentage of variance explained by each predictor as a function of latitude. In the equatorial region ($\pm 15°$), OH variance (Figure 8a) is influenced by solar forcing ($\approx$ 6–8%) with small contributions from QBO and ENSO, while Ep variance (Figure 8b) shows contributions from QBO (up to $\sim 5\%$) and modest ENSO impact. Correlations (Figure 8c–d) in the equator show: OH correlates positive with solar but near-zero with QBO and ENSO, whereas Ep shows positive correlation with QBO (30 and 50 mb) and weaker links to solar and ENSO. In the NH ($25°$–$50°$N), OH variance is dominated by solar ($\sim$ 10–15%) with little ENSO or QBO contribution, while Ep variance is split across solar, QBO, and the long-term trend, each explaining a few percent. OH is positively correlated with solar forcing, while Ep shows positive correlations with QBO and trend. In the SH ($25°$–$50°$S), OH variance is solar-driven (10–15%), with ENSO explaining a small fraction, whereas Ep variance shows trend and QBO contributions (up to 5–7%). OH links mainly to solar, while Ep shows positive associations with QBO and trend.

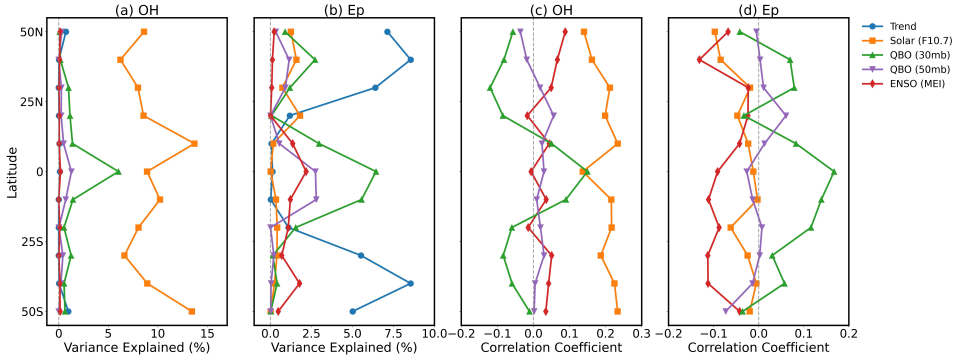

Figure 8. Latitudinal structure of the relationships between hydroxyl (OH), Ep (Ep), and climate modes. **(a, b)** Percentage of variance in deseasonalized monthly mean OH peak concentration and Ep per unit mass (Ep) at the altitude of the OH peak, respectively, explained by individual predictors. The values are derived from a multiple linear regression (MLR) model applied at each 10-degree latitude. **(c, d)** Pearson correlation coefficients between the monthly mean time series of OH peak concentration and Ep, respectively, and the climate modes. The predictors, indicated in the legend, are a linear trend (Trend), the F10.7 cm solar radio flux (Solar), the standardized Quasi-Biennial Oscillation (QBO) at 30 mb and 50 mb, and the Multivariate ENSO Index (ENSO-MEI).

3.6 Altitude-Latitude Climatology and Trends

Figure 9 presents the altitude-latitude structure of the OH and Ep climatology along with the spatial distribution of linear trends. In Figure 9a (OH_{VER}), the emission layer is largest near the mesopause around $85°$–$90°$ km, forming a maximum at the equator ($\pm 15°$) with relatively uniform latitudinal distribution but a weakening in the NH midlatitudes ($25°$–$50°$N). In the SH midlatitudes ($25°$–$50°$S), OH emissions appear somewhat more extended vertically but weaker compared to the equatorial peak. In Figure 9b (Ep, the gravity wave potential energy per unit mass), the climatology shows a broad maximum above

https://doi.org/10.5194/egusphere-2026-1038
Preprint. Discussion started: 9 March 2026
© Author(s) 2026. CC BY 4.0 License.

85° km, largest near the equator, extending well into the upper mesosphere and lower thermosphere. The equatorial region (±15°) shows the largest and vertically thickest values of Ep, while both hemispheres (25°–50°N and 25°–50°S) show weaker enhancements that do not extend as high as at the equator. The SH shows slightly larger midlatitude Ep values than the NH. In Figure 9c (linear trend slope of OH_{VER}), the equatorial region (±15°) is dominated by positive trends between 80°–95° km, indicating an intensification of OH emissions. In contrast, both hemispheres (25°–50°N and 25°–50°S) display weaker and less consistent signals: trends are largely not statistically significant, with some patches of negative slopes below 80° km and near 90° km. The SH exhibits more coherent negative trends below 80° km, whereas the NH shows smaller-scale variability without statistical significance.

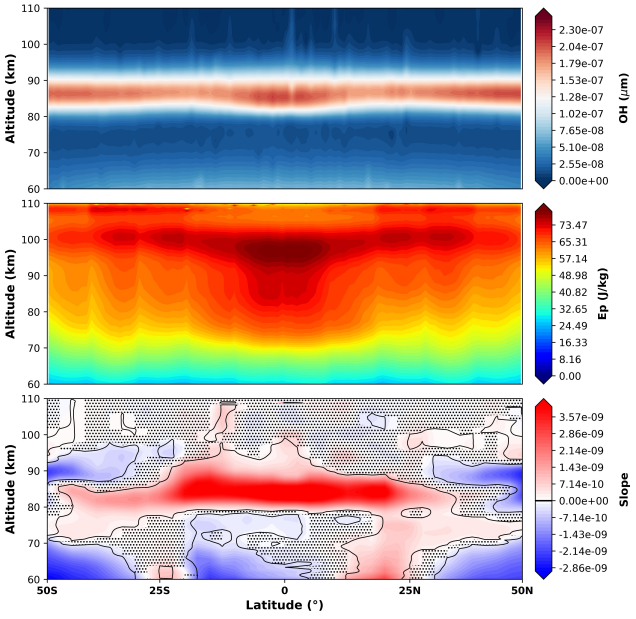

Figure 9. Climatology and linear trend. The top and middle panels show the climatological mean of OH_{VER} (in μm) and Ep (in J/Kg), respectively, as a function of latitude and altitude. The bottom panel shows the slope of the linear trend of OH_{VER}. Stippling in the bottom panel indicates regions where the trend is statistically significant at the 95% confidence level.

The altitude trends and solar responses of the OH peak (Figure 10) show the vertical structure changes of the mesospheric OH layer over the observation period. Statistical significance is indicated by blue stars ($p < 0.05$) and red stars ($p \geq 0.05$) overlaying the overall profiles, as detailed in the figure caption. In Figure 10a, the linear trend in the OH emission peak altitude is positive across all latitudes, with values around 0.02–0.04 km/year near the equatorial region (±15°). In the NH midlatitudes (25°–50°N), the overall trend increases slightly, peaking near 0.05 km/year during JJA, while DJF trends remain at ∼ 0.02 km/year. In the SH midlatitudes (25°–50°S), the trends are also positive but more seasonally contrasted: JJA trends are larger (up to ∼ 0.05–0.06 km/year), whereas DJF trends are closer to ∼ 0.01–0.02 km/year. In Figure 10b, the solar response (km/100 sfu) shows a latitude-dependent asymmetry. Near the equator (±15°), the overall response is small, close to zero, but

https://doi.org/10.5194/egusphere-2026-1038
Preprint. Discussion started: 9 March 2026
© Author(s) 2026. CC BY 4.0 License.

seasonally distinct—negative during JJA and positive to near zero during DJF. In the NH midlatitudes (25°–50°N), the overall solar response remains small but slightly positive, while JJA responses are near zero and DJF responses show negative values. By contrast, in the SH midlatitudes (25°–50°S), the overall solar response is negative, dominated by negative values during JJA, while DJF responses are closer to zero or negative.

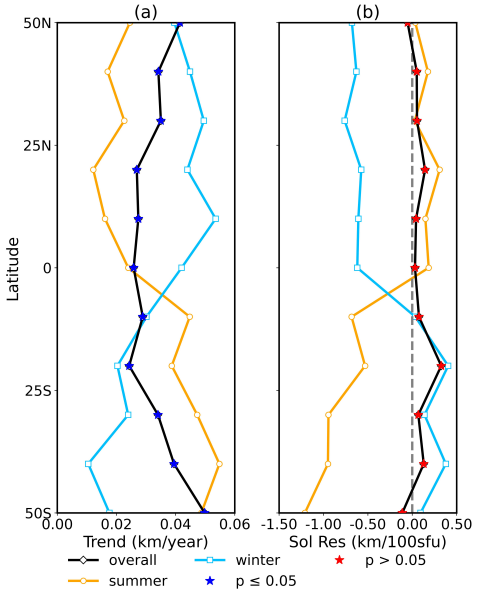

Figure 10. Latitudinal variation of (a) the linear trend in km/year and (b) the solar response (Sol Res) in km/100 sfu. The results are shown for the overall period (black line with diamonds), for JJA months (orange line with circles), and for DJF months (cyan line with squares). The vertical dashed line in panel (b) indicates zero response. The blue stars overlaying the overall profile indicate statistically significant values ($p < 0.05$), while red stars indicate values that are not statistically significant ($p \geq 0.05$).

3.7 Semiannual Oscillations and their Annual Cycles

The seasonal analysis employs harmonic decomposition techniques to extract annual oscillation (AO) and SAO components from the deseasonalized time series, following the methodology established by Gu et al. (2024) for OH airglow emission analysis. Sinusoidal functions are fitted to monthly climatological data to quantify amplitude and phase characteristics. We decompose seasonal cycles into AO and SAO components via least-squares harmonic fitting, where AO captures solar-driven annual variations and SAO represents semiannual oscillations linked to equinoctial dynamics and stratospheric circulation. The amplitude represents the magnitude of seasonal variation relative to the annual mean, while the phase indicates the timing of maximum values throughout the year, providing insights into the physical mechanisms controlling seasonal variability in mesospheric OH chemistry and gravity wave activity.

The seasonal climatology (Figure 11) reveals the annual and semi-annual patterns that drive mesospheric variability. In Figure 11a, OH_{VER} shows a semiannual cycle with equatorial maxima ($\pm 15°$) around April–May and October–November, while

https://doi.org/10.5194/egusphere-2026-1038
Preprint. Discussion started: 9 March 2026
© Author(s) 2026. CC BY 4.0 License.

minima occur during solstitial months. In the NH midlatitudes (25°–50°N), OH values are weaker overall, with enhancements in late spring and autumn. In the SH midlatitudes (25°–50°S), OH intensities are lower, though peaks are seen in May–June and November–December. In Figure 11b, Ep exhibits largest values at the equator, with broad enhancements during March–April and again in September–October, consistent with semiannual variability. In the NH (25°–50°N), Ep remains relatively weak year-round, with a faint enhancement in Boreal autumn. The SH (25°–50°S) shows similarly weak Ep values, with no distinct seasonal maxima compared to the equatorial dominance. In Figure 11c, the OH peak altitude displays a semiannual oscillation at the equator, reaching higher altitudes (∼ 83–85 km) in April–May and October–November, and lower altitudes (∼ 78–80 km) during solstitial months. In the NH (25°–50°N), the peak altitude is elevated mainly in April–May, while in the SH (25°–50°S), the main enhancement occurs during October–November. Overall, the equatorial region controls the dominant semiannual cycle, while the midlatitudes show weaker, seasonally shifted responses.

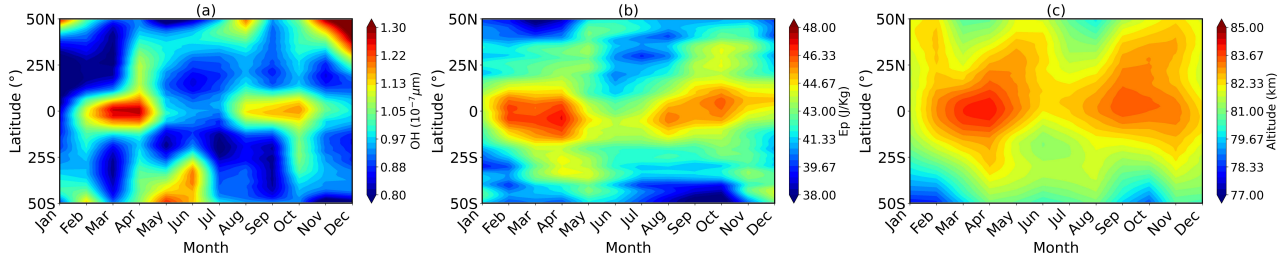

Figure 11. Mean seasonal climatology as a function of latitude and month for (a) OH_{VER} (in 10^{-7} μm), (b) Ep, Ep (in J/Kg), and (c) the altitude of the OH peak (in km).

Figure 12 shows the harmonic analysis which estimates the amplitude and phase characteristics of AO and SAO components. In the semiannual oscillation (SAO) panels (left column), OH relative amplitude (panel a) peaks at the equator (±15°) around 10–12%, while in the SH midlatitudes (25°–50°S) the amplitude reaches comparable values near 25°S but decreases further poleward. In the NH (25°–50°N), amplitudes are weaker, staying below 8%. The SAO phase indicates maxima occurring earlier in the year at higher latitudes and shifting toward later days near the equator. Ep relative amplitude (Figure 12c) also peaks in the SH (25°–50°S) with values near 4–5%, while equatorial amplitudes are weaker (∼ 2–3%), and NH values remain low (< 2%). The SAO altitude amplitude (Figure 12e) is largest at the equator, approaching ∼ 1 km, and decreases steadily toward both hemispheres, with values around 0.6 km in the midlatitudes; phases are nearly flat across latitudes.

In the annual oscillation (AO) panels (right column), OH relative amplitude (Figure 12b) shows larger signals in the SH (25°–50°S), peaking above 15–20%, while equatorial values are lower (∼ 5–7%), and the NH midlatitudes (25°–50°N) show amplitudes around 10%. Phases indicate hemispheric asymmetry, with maxima occurring later in the year in the NH compared to the SH. Ep relative amplitude (Figure 12d) exhibits alternating peaks across latitude, with larger amplitudes in the SH (∼ 3–4%), weaker equatorial values (< 2%), and NH amplitudes (∼ 2%). Finally, altitude amplitude (Figure 12f) shows equatorial suppression (∼ 0.2–0.3 km) compared to enhancements in the midlatitudes: ∼ 0.6 km in the SH (25°–50°S) and ∼ 0.4–0.5 km

https://doi.org/10.5194/egusphere-2026-1038
Preprint. Discussion started: 9 March 2026
© Author(s) 2026. CC BY 4.0 License.

in the NH (25°–50°N). AO phases are more variable, reflecting hemispheric differences and less coherent timing compared to the SAO.

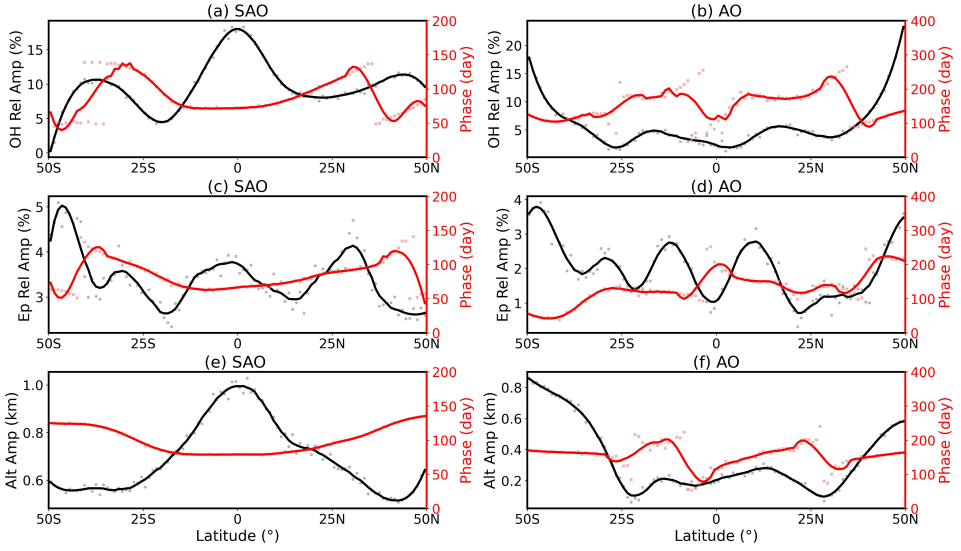

Figure 12. Latitudinal variations of the amplitude (black lines, left axes) and phase (red lines, right axes) for the (left column) SAO and (right column) AO. The rows correspond to different parameters: (a, b) OH relative amplitude (%), (c, d) Ep relative amplitude (%), and (e, f) Altitude amplitude (km). Phase represents the day of maximum and is given in days. The faint points (gray circles for amplitude, red squares for phase) represent the binned data, while the solid lines are smoothed fits.

3.8 Thermal and Non-Thermal Contributions of OH Trend

The decomposition analysis separates temperature-driven effects from residual non-thermal processes in OH variability. The methodology integrates SABER satellite observations with geophysical indices representing atmospheric drivers (F10.7, Kp, MEI, QBO) using a two-stage MLR framework. After aggregating data into 10-degree latitude bins and removing seasonal periodicities, the deseasonalized anomalies are modeled using:

$$Y(t) = C_0 + C_1 \cdot t + \sum_{i=2}^{N} C_i \cdot P_i(t) + \epsilon(t) \tag{9}$$

where $Y(t)$ represents OH or temperature, C_1 is the linear trend coefficient, $P_i(t)$ are the geophysical proxies, and $\epsilon(t)$ is residual variability. The decomposition leverages the temperature dependence of OH chemistry. The temperature-driven component of OH trends is calculated as:

$$\text{Trend}_{OH,Temp} = \overline{OH} \cdot \beta \cdot \text{Trend}_{Temp} \tag{10}$$

Where β is the temperature sensitivity coefficient, the residual trend is then isolated as:

$$\text{Trend}_{OH,Res} = \text{Trend}_{OH,Obs} - \text{Trend}_{OH,Temp} \tag{11}$$

https://doi.org/10.5194/egusphere-2026-1038
Preprint. Discussion started: 9 March 2026
© Author(s) 2026. CC BY 4.0 License.

This decomposition is applied to both trends and responses to each proxy, providing quantitative separation of thermal versus non-thermal mechanisms. Figure 13 presents the decomposition of OH trends and the correlation between OH and temperature trends. In Figure 13a, the observed OH trend is negative across all latitudes. At the equator ($\pm 15°$), OH trends are close to zero, showing weak decreases. In the NH (25°–50°N), the trend is negative, ranging between -1 and -3×10^{-10} μm/yr, while in the SH (25°–50°S) the decline reaches values near -4 to -5×10^{-10} μm/yr. Figure 13b shows that temperature trends at the OH peak altitude are negative across latitudes, with the cooling (~ -0.15 K/yr) near the equator, weakening toward the midlatitudes in both hemispheres, where values range around -0.07 to -0.1 K/yr. Figure 13c shows the decomposition of the OH trend: the temperature-driven component (green) accounts for most of the negative signal, especially at the equator ($\pm 15°$) and in the SH (25°–50°S). A positive residual component (purple) emerges across latitudes, partly offsetting the cooling effect. This residual is larger in the midlatitudes of both hemispheres, suggesting additional drivers beyond temperature sustain OH emission levels despite the cooling background.

The correlation coefficient between the OH and temperature trends (Figure 13d) ranges from -0.25 to 0.5. Peak values of 0.4–0.5 occur in several latitude bands, consistent with the temperature dependence of the H + O_3 reaction rate. The correlation reaches a minimum of -0.25 near 25°N, indicating an anti-correlation in the Northern Hemisphere subtropics. This sign reversal points to non-thermal processes, such as changes in the Brewer–Dobson circulation or hemispheric asymmetries in wave-driven transport, that oppose the thermochemical response. Away from this minimum, the correlation returns to positive values but remains below 0.5 at all latitudes, indicating that non-thermal contributions persist across the globe. The correlation analysis in Figure 13d thus complements the decomposition in Figure 13c, confirming that thermal effects account for only part of the OH trend and that non-thermal processes dominate in the Northern Hemisphere subtropics.

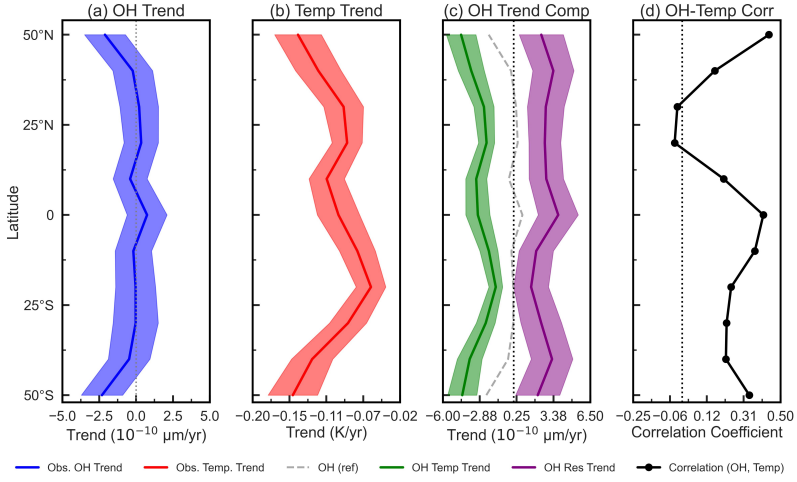

Figure 13. Decomposition of the linear trend in OH_{VER} and its correlation with temperature. (a) The observed latitudinal profile of the OH trend. (b) The observed latitudinal profile of the temperature trend at the OH peak altitude. (c) The observed OH trend (dashed gray) is decomposed into a component driven by the temperature trend (green) and a residual trend (purple). (d) The correlation coefficient between the OH and temperature trends. Shaded areas indicate the uncertainty.

https://doi.org/10.5194/egusphere-2026-1038
Preprint. Discussion started: 9 March 2026
© Author(s) 2026. CC BY 4.0 License.

4 Discussion

The observed correlation coefficients of 0.3–0.7 between OH VER and gravity wave Ep (Figure 8) confirm the coupling mechanisms proposed by Li et al. (2011) and Tarasick and Shepherd (1992). The physical basis involves gravity wave-induced temperature perturbations modulating the OH production rate through the $H + O_3 \rightarrow OH^* + O_2$ reaction (Minschwaner et al., 2011). Early dynamical-chemical modelling by Walterscheid et al. (1987) and Schubert et al. (1991) predicted that gravity waves should produce correlated fluctuations in OH nightglow brightness and rotational temperature, a prediction now confirmed observationally over a 22-year baseline. The DJF enhancement of correlations at mid-latitudes (reaching 0.7) arises because longer vertical wavelength waves during winter produce temperature perturbations that remain coherent across the OH emission layer, minimizing destructive interference (Taylor et al., 2009; Ejiri et al., 2003; Nielsen et al., 2009). Conversely, the weaker equatorial correlations ($\sim$0.3) are consistent with the dominance of shorter vertical wavelength convectively generated waves in the tropics, whose phase structure can produce cancellation across the $\sim$8 km-thick OH layer (Vargas et al., 2007; Fritts and Alexander, 2003).

The solar response (Figure 5) shows OH responds positively across all latitudes with an equatorial maximum of 0.8–1.0 $\times$ 10^{-7} W m^{-3} per 100 sfu, arising from Lyman-α photo-dissociation of H_2O producing atomic hydrogen for OH production (Mlynczak et al., 2013). Solar forcing explains 10–15% of OH variance at mid-latitudes (Figure 8) (Gao et al., 2010; Fytterer et al., 2015). Gravity wave Ep shows weaker solar responses with hemispheric asymmetries: increased solar activity strengthens the polar vortex, reducing wave propagation efficiency in the NH during DJF (Liu et al., 2017; Ern et al., 2017). This asymmetry is consistent with the mechanism described by Lieberman et al. (2013), whereby stratospheric planetary waves selectively filter gravity waves, and the filtering efficiency varies with the strength of the background zonal wind, which itself responds to the solar cycle.

The QBO response (Figure 6) shows an equatorial-midlatitude dipole, with QBO30 producing positive OH responses at the equator while QBO50 yields negative values. The 30 mb index produces larger responses because upper stratospheric winds control critical level filtering of gravity waves (Dunkerton, 1997; Baldwin et al., 2001; Holton and Tan, 1980; Marsh et al., 2006). The ENSO response (Figure 7) shows negative OH values across all latitudes (maximum -3.72×10^{-7} W m^{-3}/MEI at 50°S) coupled with positive Ep responses (maximum 0.21 J kg^{-1}/MEI at 50°N). During El Niño, altered convection modifies planetary wave propagation, weakening the polar vortex and reducing atomic hydrogen transport while enhancing gravity wave generation (Baldwin et al., 2001; Randel et al., 2009; Sassi et al., 2004; Fernández et al., 2004). The opposing signs of the OH and Ep ENSO responses are noteworthy: enhanced convective activity during El Niño generates additional gravity waves that propagate into the mesosphere (Bramberger et al., 2017), yet the accompanying changes in the Brewer–Dobson circulation reduce the downward transport of atomic oxygen, thereby suppressing OH production despite the increased wave forcing.

The trend analysis (Figures 4 and 9) shows contrasting patterns: OH exhibits negative trends at mid-latitudes (-1 to -5×10^{-10} W m^{-3} yr^{-1}) with weaker trends near the equator, while Ep shows positive trends at mid-latitudes (2.7–5.3 $\times$ 10^{-2} J kg^{-1} yr^{-1}). The positive OH peak altitude trends of 0.02–0.06 km/year (Figure 10) indicate upward shift consistent with mesospheric cooling under increasing CO_2 (Beig et al., 2003; Laštovička et al., 2006; Akmaev et al., 2006). This up-

https://doi.org/10.5194/egusphere-2026-1038
Preprint. Discussion started: 9 March 2026
© Author(s) 2026. CC BY 4.0 License.

ward migration of the OH layer is in agreement with the long-term mesopause temperature and altitude trends reported by Yuan et al. (2019) from Na lidar observations, and with the broader pattern of upper-atmospheric contraction reviewed by Laštovička (2017). Recent analyses of 22 years of SABER temperature data have further revealed the near-global occurrence of mesospheric inversion layers that modulate the local thermal structure and can influence the vertical propagation of gravity waves (Ayorinde et al., 2026). The positive Ep trends exceed predictions from wave generation models, which typically predict increases of 1–2% per decade based on enhanced tropospheric convection (Geller et al., 2013; Alexander et al., 2010); our observed trends of 2–4% per decade suggest additional mechanisms such as reduced wave dissipation due to altered background winds or enhanced wave generation from non-convective sources. The modification of gravity wave parameterisations in whole-atmosphere models, as explored by Garcia et al. (2017), may need to account for these larger-than-expected trends to accurately reproduce the observed mesospheric variability.

The decomposition analysis (Figure 13) separates temperature-driven from non-thermal processes and constitutes a central result of this study. Temperature trends range from -0.07 to -0.15 K/yr, with the temperature-driven component accounting for most OH decreases (Yue et al., 2019; Emmert et al., 2010). The negative temperature trends are consistent with the radiative cooling expected from increasing CO_2 concentrations in the mesosphere (Akmaev et al., 2006; Yue et al., 2015), and the resulting OH decreases follow directly from the temperature dependence of the $H + O_3$ reaction rate constant, which decreases by approximately 2–3 % per Kelvin of cooling at mesospheric temperatures (Sander et al., 2011; Atkinson et al., 2006).

Positive mid-latitude residuals indicate additional non-thermal dynamical mechanisms, including altered atomic oxygen or water vapor transport due to changes in mesospheric circulation. Several processes may contribute to these residuals. First, long-term changes in the Brewer–Dobson circulation can modify the downward flux of atomic oxygen into the mesopause region, altering the O_3 production that feeds the $H + O_3$ reaction (Shepherd et al., 2014; Smith, 2012). Second, secular changes in gravity wave momentum deposition, evidenced by the positive Ep trends documented here, can alter the residual mean meridional circulation, redistributing chemical species independently of local temperature changes (Garcia et al., 2017; Fritts and Alexander, 2003). Third, long-term increases in mesospheric water vapour, potentially linked to methane oxidation, could enhance OH production through increased hydrogen radical availability (Yue et al., 2019). The fact that the residual component is larger in the NH subtropics, where the OH–temperature correlation reaches its minimum of -0.25 near $25°$N (Figure 13d), suggests that hemispheric asymmetries in wave-driven transport play a particularly important role at these latitudes.

Solar forcing operates primarily through thermal pathways, whereas QBO and ENSO responses exhibit larger dynamical components driven by wave-mean flow interactions (Garcia et al., 2017; Ayorinde et al., 2025; Hickey et al., 1997; Snively, 2013). The predominantly non-thermal character of the QBO response is consistent with the mechanism of selective gravity wave filtering by QBO-modulated stratospheric winds (Dunkerton, 1997; Ayorinde et al., 2025): changes in the stratospheric wind profile alter which gravity waves reach the mesosphere, modifying the momentum deposition and chemical transport patterns without requiring local temperature changes. Similarly, the ENSO-driven non-thermal response reflects the teleconnection pathway whereby tropical convective anomalies modify planetary wave propagation into the stratosphere, altering the filtering environment for gravity waves and the strength of the residual circulation (Sassi et al., 2004; Calvo et al., 2010). These findings underscore that mesospheric OH variability cannot be understood through photochemistry alone; dynamical transport

https://doi.org/10.5194/egusphere-2026-1038
Preprint. Discussion started: 9 March 2026
© Author(s) 2026. CC BY 4.0 License.

and wave-driven circulation changes are essential components of the response to both natural variability modes and long-term climate forcing.

The harmonic analysis (Figures 11 and 12) shows semiannual oscillations dominate at the equator (OH amplitude 10-12%) while annual oscillations peak in the SH midlatitudes (OH amplitude 15-20%). The equatorial SAO reflects mesospheric circulation reversal during equinoxes (Gu et al., 2024; Garcia et al., 2014). The stronger AO amplitudes in the SH arise from hemispheric differences in planetary wave activity (Baldwin et al., 2001; Alexander et al., 2010). These patterns provide observational constraints for atmospheric models (Marsh et al., 2006; Garcia et al., 2014; Sato et al., 2009).

5 Conclusions

This study presents a comprehensive 22-year (2002–2023) analysis of mesospheric OH airglow and gravity wave potential energy (Ep) using TIMED/SABER observations, providing one of the longest continuous records of coupled chemistry–dynamics variability in the mesosphere. The principal findings are as follows.

- OH emissions and gravity wave Ep are positively correlated across all latitudes, with correlation coefficients of 0.3–0.7 ($p < 0.05$) that peak during winter months at mid-latitudes. This coupling operates through both thermal modulation of the $H + O_3$ reaction rate and dynamical advection of reactive species by gravity waves.

- OH emissions exhibit negative trends at mid-latitudes in both hemispheres (-1 to -5×10^{-10} W m^{-3} yr^{-1}), consistent with mesospheric cooling under increasing CO_2, while gravity wave Ep shows positive trends at mid-latitudes (up to 5.3×10^{-2} J kg^{-1} yr^{-1}) that exceed current model predictions of 1–2 % per decade. Both quantities show weaker trends near the equator, and the OH peak altitude is rising at 0.02–0.06 km yr^{-1}, further corroborating long-term mesospheric cooling.

- Solar variability explains approximately 10–15 % of OH variance at mid-latitudes, operating primarily through Lyman-α photodissociation of H_2O and subsequent thermal pathways. The solar response in Ep is weaker and exhibits hemispheric asymmetries linked to polar vortex modulation of wave propagation.

- QBO and ENSO responses demonstrate that tropical atmospheric variability propagates to mesospheric altitudes. The 30 mb QBO index produces larger OH responses than the 50 mb index, indicating upper-stratospheric wind control of gravity wave critical-level filtering. ENSO drives negative OH responses across all latitudes while simultaneously enhancing Ep, revealing opposing chemical and dynamical pathways.

- The novel decomposition methodology reveals that temperature-driven components account for the majority of observed OH trends, particularly the cooling-induced decreases at the equator and in the Southern Hemisphere. However, positive residual (non-thermal) components emerge at mid-latitudes in both hemispheres, and the OH–temperature correlation reaches a minimum of -0.25 near 25°N, indicating that non-thermal processes, including Brewer–Dobson circulation

https://doi.org/10.5194/egusphere-2026-1038
Preprint. Discussion started: 9 March 2026
© Author(s) 2026. CC BY 4.0 License.

changes and hemispheric asymmetries in wave-driven transport, dominate over thermal effects in the Northern Hemisphere subtropics. Solar responses are predominantly thermal, whereas QBO and ENSO responses exhibit larger non-thermal dynamical components.

These results provide observational constraints for atmospheric models, specifically for gravity wave parameterisations and mesospheric photochemistry schemes, and highlight the critical role of chemistry–dynamics coupling in mesospheric climate responses. The 22-year dataset establishes a benchmark for evaluating model representations of middle atmospheric variability under evolving climate conditions.

Data availability. TIMED/SABER Level 2A data are publicly available through the NASA Goddard Earth Sciences Data and Information Services Center (GES DISC) at https://disc.gsfc.nasa.gov/. Solar flux (F10.7) data are available from the National Research Council of Canada at https://spaceweather.gc.ca/. QBO wind data are provided by the Free University of Berlin at https://www.geo.fu-berlin.de/en/met/ag/strat/produkte/qbo/. MEI data are available from NOAA at https://psl.noaa.gov/enso/mei/. Geomagnetic indices are provided by GFZ at https://kp.gfz-potsdam.de/. Processed datasets and analysis codes used in this study are available upon request from the corresponding author.

Author contributions. Conceptualisation, T. T. A., C. M. W., and H. T.; methodology, T. T. A.; software, T. T. A.; validation, C. M. W. and H. T.; formal analysis, T. T. A.; investigation, T. T. A.; data curation, T. T. A.; writing-original draft preparation, T. T. A.; writing, review and editing, T. T. A., C. M. W., H. T., L. F. R. V., A. V. B., and C. A. O. B. F.; visualization, G. A. G., A. V. B., and L. F. R. V.; supervision, C. M. W. and H. T.; project administration, T. T. A.; funding acquisition, C. M. W.

Competing interests. The authors declare that there are no competing interests.

Acknowledgements. The authors thank the TIMED/SABER team for providing the high-quality atmospheric observations that made this study possible. The authors acknowledge CDAAC, ECMWF, and NOAA for providing the data. T. T. Ayorinde acknowledges the Conselho Nacional de Desenvolvimento Científico e Tecnológico (CNPq) under the process numbers $303871/2023-7$. C. M. Wrasse acknowledges the financial support provided by the Brazilian Ministry of Science, Technology, and Innovations (MCTI) and the Brazilian Space Agency (AEB) under the grant number $20VB.0009$ and the CNPq under the process numbers $141373/2019-9$. L.F.R. Vital acknowledges the China–Brazil Joint Laboratory for Space Weather (CBJLSW), the National Space Science Center (NSSC), and the Chinese Academy of Sciences (CAS) for supporting his postdoctoral fellowship. This research was also supported by the Deployment Project of the Overseas Science and Education Cooperation Center, Bureau of International Cooperation, Chinese Academy of Sciences (Grant No. 119GJHZ2024027MI). A. V. Bilibio. acknowledges Fundação de Apoio à Pesquisa do Estado da Paraíba - FAPESQ (Grant No. 72736.1300.35596.03012025). H. Takahashi. Ayorinde acknowledges the Conselho Nacional de Desenvolvimento Científico e Tecnológico (CNPq) under the process numbers

https://doi.org/10.5194/egusphere-2026-1038
Preprint. Discussion started: 9 March 2026
© Author(s) 2026. CC BY 4.0 License.

303871/2023−7. C. A. O. B. Figueiredo would like to express his gratitude to the CNPq for their support and funding number 307986/2025-0.

https://doi.org/10.5194/egusphere-2026-1038
Preprint. Discussion started: 9 March 2026
© Author(s) 2026. CC BY 4.0 License.

References

Akmaev, R. A., Fomichev, V. I., and Zhu, X.: Impact of middle-atmospheric composition changes on greenhouse cooling in the upper atmosphere, Journal of Atmospheric and Solar-Terrestrial Physics, 68, 1879–1889, https://doi.org/10.1016/j.jastp.2006.03.008, 2006.

Alexander, M. J., Geller, M., McLandress, C., Polavarapu, S., Preusse, P., Sassi, F., Sato, K., Eckermann, S., Ern, M., Hertzog, A., Kawatani, Y., Pulido, M., Shaw, T. A., Sigmond, M., Vincent, R., and Watanabe, S.: Recent developments in gravity-wave effects in climate models and the global distribution of gravity-wave momentum flux from observations and models, Quarterly Journal of the Royal Meteorological Society, 136, 1103–1124, https://doi.org/10.1002/qj.637, 2010.

Anderson, J. L., Liu, H.-L., and Raeder, K.: Interhemispheric differences of mesosphere–lower thermosphere winds and tides investigated from three whole atmosphere models and meteor radar observations, Atmospheric Chemistry and Physics, 21, 13 855–13 902, https://doi.org/10.5194/acp-21-13855-2021, 2021.

Atkinson, R., Baulch, D. L., Cox, R. A., Crowley, J. N., Hampson, R. F., Hynes, R. G., Jenkin, M. E., Rossi, M. J., and Troe, J.: Evaluated kinetic and photochemical data for atmospheric chemistry: Volume II – gas phase reactions of organic species, Atmospheric Chemistry and Physics, 6, 3625–4055, https://doi.org/10.5194/acp-6-3625-2006, 2006.

Ayorinde, T. T., Wrasse, C. M., Takahashi, H., Figueiredo, C. A. O. B., Barros, D., Lomotey, S. O., Essien, P., and Bilibio, A. V.: Stratospheric gravity wave potential energy and tropospheric parameters relationships over South America: a study using COSMIC-2 and METOP radio occultation measurements, Earth, Planets and Space, 75, 136, https://doi.org/10.1186/s40623-023-01891-8, 2023.

Ayorinde, T. T., Wrasse, C. M., Takahashi, H., Barros, D., Figueiredo, C. A. O. B., da Silva, L. A., and Bilibio, A. V.: Investigation of the long-term variation of gravity waves over South America using empirical orthogonal function analysis, Earth, Planets and Space, 76, 105, https://doi.org/10.1186/s40623-024-02045-0, 2024.

Ayorinde, T. T., Wrasse, C. M., Takahashi, H., Barros, D., Figueiredo, C. A. O. B., Essien, P., and Bilibio, A. V.: Modulation of tropical stratospheric gravity wave activity and the ITCZ position by climate variability modes, Atmospheric Chemistry and Physics, 25, 12 357–12 380, https://doi.org/10.5194/acp-25-12357-2025, 2025.

Ayorinde, T. T., Wrasse, C. M., Agyei-Yeboah, E., Takahashi, H., Figueiredo, C. A. O. B., Barros, D., Bilibio, A. V., and Vital, L. F. R.: Near-Global Occurrences of Mesospheric Inversion Layers Observed from 22 Years of TIMED/SABER Temperature Measurements, Journal of Climate, 39, 903–923, https://doi.org/10.1175/JCLI-D-25-0140.1, 2026.

Baldwin, M. P., Gray, L. J., Dunkerton, T. J., Hamilton, K., Haynes, P. H., Randel, W. J., Holton, J. R., Alexander, M. J., Hirota, I., Horinouchi, T., Jones, D. B. A., Kinnersley, J. S., Marquardt, C., Sato, K., and Takahashi, M.: The quasi-biennial oscillation, Reviews of Geophysics, 39, 179–229, https://doi.org/10.1029/1999RG000073, 2001.

Beig, G., Keckhut, P., Lowe, R. P., Roble, R. G., Mlynczak, M. G., Scheer, J., Fomichev, V. I., Offermann, D., French, W. J. R., Shepherd, M. G., Semenov, A. I., Remsberg, E. E., She, C. Y., Lübken, F.-J., Bremer, J., Clemesha, B. R., Stegman, J., Sigernes, F., and Fadnavis, S.: Review of mesospheric temperature trends, Reviews of Geophysics, 41, 1015, https://doi.org/10.1029/2002RG000121, 2003.

Bramberger, M., Dörnbrack, A., Gisinger, S., Kaifler, B., Kaifler, N., Rapp, M., Witschas, B., and Zagar, N.: Does strong tropospheric forcing cause large-amplitude mesospheric gravity waves? A DEEPWAVE case study, Journal of Geophysical Research: Atmospheres, 122, 11,970–11,993, https://doi.org/10.1002/2017JD027371, 2017.

Calvo, N., Marsh, D. R., Garcia-Herrera, R., García, R. R., and Giorgetta, M. A.: Analysis of the ENSO signal in tropospheric and stratospheric temperatures observed by MSU, 1979–2000, Journal of Climate, 23, 309–324, https://doi.org/10.1175/2009JCLI2934.1, 2010.

https://doi.org/10.5194/egusphere-2026-1038
Preprint. Discussion started: 9 March 2026
© Author(s) 2026. CC BY 4.0 License.

Dunkerton, T. J.: The role of gravity waves in the quasi-biennial oscillation, Journal of Geophysical Research, 102, 26 053–26 076, https://doi.org/10.1029/96JD02999, 1997.

Ejiri, M. K., Shiokawa, K., Ogawa, T., Igarashi, K., Nakamura, T., and Tsuda, T.: Statistical study of short-period gravity waves in OH and OI nightglow images at two separated sites, Journal of Geophysical Research, 108, 4679, https://doi.org/10.1029/2002JD002795, 2003.

Emmert, J. T., Lean, J. L., and Picone, J. M.: Record-low thermospheric density during the 2008 solar minimum, Geophysical Research Letters, 37, L12 102, https://doi.org/10.1029/2010GL043671, 2010.

Ern, M., Preusse, P., Gille, J. C., Hepplewhite, C. L., Mlynczak, M. G., Russell III, J. M., and Riese, M.: Implications for atmospheric dynamics derived from global observations of gravity wave momentum flux in stratosphere and mesosphere, Journal of Geophysical Research: Atmospheres, 116, D19 107, https://doi.org/10.1029/2011JD015821, 2011.

Ern, M., Hoffmann, L., and Preusse, P.: Directional gravity wave momentum fluxes in the stratosphere derived from high-resolution AIRS temperature data, Geophysical Research Letters, 44, 475–485, https://doi.org/10.1002/2016GL072007, 2017.

Fernández, N. C., Herrera, R. G., Puyol, D. G., MartÍn, E. H., GarcÍa, R. R., Presa, L. G., and RodrÍguez, P. R.: Analysis of the ENSO signal in tropospheric and stratospheric temperatures observed by MSU, 1979–2000, Journal of climate, 17, 3934–3946, https://doi.org/10.1175/1520-0442(2004)017<3934:AOTESI>2.0.CO;2, 2004.

Fritts, D. C. and Alexander, M. J.: Gravity wave dynamics and effects in the middle atmosphere, Reviews of Geophysics, 41, 1003, https://doi.org/10.1029/2001RG000106, 2003.

Fytterer, T., Sinnhuber, M., Funke, B., López-Puertas, M., Stiller, G., von Clarmann, T., and Wissing, J. M.: The 27 day solar rotational effect on mesospheric nighttime OH and O3 observations, Journal of Geophysical Research: Space Physics, 120, 7071–7081, https://doi.org/10.1002/2015JA021183, 2015.

Gao, H., Xu, J., Smith, A. K., Mlynczak, M. G., and Russell III, J. M.: Seasonal and QBO variations in the OH nightglow emission observed by TIMED/SABER, Journal of Geophysical Research: Space Physics, 115, A06 313, https://doi.org/10.1029/2009JA014641, 2010.

Gao, H., Xu, J., Ward, W., and Smith, A. K.: Temporal evolution of nightglow emission responses to SSW events observed by TIMED/SABER, Journal of Geophysical Research: Atmospheres, 116, https://doi.org/10.1029/2011JD015936, 2011.

Garcia, R. R., López-Puertas, M., Funke, B., Marsh, D. R., Kinnison, D. E., Smith, A. K., and González-Galindo, F.: On the distribution of CO_2 and CO in the mesosphere and lower thermosphere, Journal of Geophysical Research: Atmospheres, 119, 5700–5718, https://doi.org/10.1002/2013JD021208, 2014.

Garcia, R. R., Smith, A. K., Kinnison, D. E., Cámara, Á. d. l., and Murphy, D. J.: Modification of the gravity wave parameterization in the Whole Atmosphere Community Climate Model: Motivation and results, Journal of the Atmospheric Sciences, 74, 275–291, https://doi.org/10.1175/JAS-D-16-0104.1, 2017.

Geller, M. A., Alexander, M. J., Love, P. T., Bacmeister, J., Ern, M., Hertzog, A., Manzini, E., Preusse, P., Sato, K., Scaife, A. A., and Zhou, T.: A comparison between gravity wave momentum fluxes in observations and climate models, Journal of Climate, 26, 6383–6405, https://doi.org/10.1175/JCLI-D-12-00545.1, 2013.

Gu, S.-Y., Wang, D., Qin, Y., Tang, L., Wei, Y., and Dou, X.: Semiannual oscillation, annual oscillation, quasibiennial oscillation, and solar cycle variation of the OH airglow emission in the mesopause region, Earth and Planetary Physics, 8, 479–496, https://doi.org/10.26464/epp2024026, 2024.

Hickey, M. P., Walterscheid, R. L., Taylor, M. J., Ward, W., Schubert, G., Zhou, Q., Garcia, F., Kelley, M. C., and Shepherd, G. G.: Numerical simulations of gravity waves imaged over Arecibo during the 10-day January 1993 campaign, Journal of Geophysical Research: Atmospheres, 102, 11 475–11 489, https://doi.org/10.1029/97JA00181, 1997.

https://doi.org/10.5194/egusphere-2026-1038
Preprint. Discussion started: 9 March 2026
© Author(s) 2026. CC BY 4.0 License.

Holton, J. R. and Tan, H.-C.: The influence of the equatorial quasi-biennial oscillation on the global circulation at 50 mb, Journal of the Atmospheric Sciences, 37, 2200–2208, https://doi.org/10.1175/1520-0469(1980)037<2200:TIOTEQ>2.0.CO;2, 1980.

Laštovička, J.: A review of recent progress in trends in the upper atmosphere, Journal of Atmospheric and Solar-Terrestrial Physics, 163, 2–13, https://doi.org/10.1016/j.jastp.2017.03.009, 2017.

Laštovička, J., Akmaev, R. A., Beig, G., Bremer, J., and Emmert, J. T.: Global change in the upper atmosphere, Science, 314, 1253–1254, https://doi.org/10.1126/science.1135134, 2006.

Lean, J. L.: Estimating solar irradiance since 850 CE, Earth and Space Science, 5, 133–149, https://doi.org/10.1002/2017EA000357, 2018.

Li, Z., Liu, A. Z., Lu, X., Swenson, G. R., and Franke, S. J.: Gravity wave characteristics from OH airglow imager over Maui, Journal of Geophysical Research: Atmospheres, 116, https://doi.org/10.1029/2011JD015870, 2011.

Lieberman, R., Riggin, D., and Siskind, D.: Stationary waves in the wintertime mesosphere: Evidence for gravity wave filtering by stratospheric planetary waves, Journal of Geophysical Research: Atmospheres, 118, 3139–3149, https://doi.org/10.1002/jgrd.50319, 2013.

Liu, X., Yue, J., Xu, J., Garcia, R. R., Russell III, J. M., Mlynczak, M., Wu, D. L., and Nakamura, T.: Variations of global gravity waves derived from 14 years of SABER temperature observations, Journal of Geophysical Research: Atmospheres, 122, 6231–6249, https://doi.org/10.1002/2017JD026604, 2017.

Marsh, D. R., Smith, A. K., Mlynczak, M. G., and Russell III, J. M.: SABER observations of the OH Meinel airglow variability near the mesopause, Journal of Geophysical Research: Space Physics, 111, A10S05, https://doi.org/10.1029/2005JA011451, 2006.

Matzka, J., Stolle, C., Yamazaki, Y., Bronkalla, O., and Morschhauser, A.: The geomagnetic Kp index and derived indices of geomagnetic activity, Space Weather, 19, e2020SW002 641, https://doi.org/10.1029/2020SW002641, 2021.

Minschwaner, K., Manney, G., Wang, S., and Harwood, R.: Hydroxyl in the stratosphere and mesosphere–Part 1: Diurnal variability, Atmospheric Chemistry and Physics, 11, 955–962, https://doi.org/10.5194/acp-11-955-2011, 2011.

Mlynczak, M. G.: Energetics of the mesosphere and lower thermosphere and the SABER experiment, Advances in Space Research, 20, 1177–1183, https://doi.org/10.1016/S0273-1177(97)00769-2, 1997.

Mlynczak, M. G., Martin-Torres, F. J., Crowley, G., Kratz, D. P., Funke, B., Lu, G., Lopez-Puertas, M., Russell III, J. M., Kozyra, J., Mertens, C., et al.: Energy transport in the thermosphere during the solar storms of April 2002, Journal of Geophysical Research: Space Physics, 110, https://doi.org/10.1029/2005JA011141, 2005.

Mlynczak, M. G., Hunt, L. A., Mast, J. C., Marshall, B. T., Russell III, J. M., Smith, A. K., Siskind, D. E., Yee, J.-H., Mertens, C. J., Martin-Torres, F. J., Thompson, R. E., Drob, D. P., and Gordley, L. L.: Atomic oxygen in the mesosphere and lower thermosphere derived from SABER: Algorithm theoretical basis and measurement uncertainty, Journal of Geophysical Research: Atmospheres, 118, 5724–5735, https://doi.org/10.1002/jgrd.50401, 2013.

Newman, P. A., Coy, L., Pawson, S., and Lait, L. R.: The anomalous change in the QBO in 2015-2016, Geophysical Research Letters, 43, 8791–8797, https://doi.org/10.1002/2016GL070373, 2016.

Nielsen, K., Taylor, M. J., Hibbins, R., and Jarvis, M.: Climatology of short-period mesospheric gravity waves over Halley, Antarctica (76 S, 27 W), Journal of Atmospheric and Solar-Terrestrial Physics, 71, 991–1000, https://doi.org/10.1016/j.jastp.2009.04.005, 2009.

Offermann, D., Hoffmann, P., Knieling, P., Koppmann, R., Oberheide, J., and Steinbrecht, W.: Long-term trends and solar cycle variations of mesospheric temperature and dynamics, Journal of Geophysical Research: Atmospheres, 115, 2010.

Randel, W. J., Garcia, R. R., Calvo, N., and Marsh, D.: ENSO influence on zonal mean temperature and ozone in the tropical lower stratosphere, Geophysical Research Letters, 36, L15 822, https://doi.org/10.1029/2009GL039343, 2009.

https://doi.org/10.5194/egusphere-2026-1038
Preprint. Discussion started: 9 March 2026
© Author(s) 2026. CC BY 4.0 License.

Remsberg, E. E., Marshall, B. T., Garcia-Comas, M., Krueger, D., Lingenfelser, G. S., Martin-Torres, J., Mlynczak, M. G., Russell III, J. M., Smith, A. K., Zhao, Y., Brown, C., Gordley, L. L., Lopez-Gonzalez, M. J., Lopez-Puertas, M., She, C.-Y., Taylor, M. J., and Thompson, R. E.: Assessment of the quality of the Version 1.07 temperature-versus-pressure profiles of the middle atmosphere from TIMED/SABER, Journal of Geophysical Research: Atmospheres, 113, D17 101, https://doi.org/10.1029/2008JD010013, 2008.

Richards, P., Fennelly, J. a., and Torr, D.: EUVAC: A solar EUV flux model for aeronomic calculations, Journal of Geophysical Research: Space Physics, 99, 8981–8992, https://doi.org/10.1029/94JA00518, 1994.

Russell III, J. M., Mlynczak, M. G., Gordley, L. L., Tansock Jr., J. J., and Esplin, R. W.: Overview of the SABER experiment and preliminary calibration results, Proceedings of SPIE, 3756, 277–288, https://doi.org/10.1117/12.366382, 1999.

Sander, S. P., Abbatt, J., Barker, J. R., Burkholder, J. B., Friedl, R. R., Golden, D. M., Huie, R. E., Kolb, C. E., Kurylo, M. J., Moortgat, G. K., Orkin, V. L., and Wine, P. H.: Chemical Kinetics and Photochemical Data for Use in Atmospheric Studies, Evaluation No. 17, JPL Publication, 10-6, 1–408, 2011.

Sassi, F., Kinnison, D., Boville, B. A., Garcia, R. R., and Roble, R.: Effect of El Niño–Southern Oscillation on the dynamical, thermal, and chemical structure of the middle atmosphere, Journal of Geophysical Research, 109, D17 108, https://doi.org/10.1029/2003JD004434, 2004.

Sato, K., Watanabe, S., Kawatani, Y., Tomikawa, Y., Miyazaki, K., and Takahashi, M.: On the origins of mesospheric gravity waves, Geophysical Research Letters, 36, L19 801, https://doi.org/10.1029/2009GL039908, 2009.

Schubert, G., Walterscheid, R. L., and Hickey, M. P.: Gravity wave-driven fluctuations in OH nightglow, Journal of Geophysical Research: Space Physics, 96, 13 869–13 880, https://doi.org/10.1029/91JA01217, 1991.

Shepherd, M. G., Beagley, S. R., and Fomichev, V. I.: Stratospheric warming influence on the mesosphere/lower thermosphere as seen by the extended Canadian Middle Atmosphere Model, Annales Geophysicae, 32, 447–457, https://doi.org/10.5194/angeo-32-447-2014, 2014.

Sivakandan, M., Ramkumar, T., Taori, A., Rao, V., and Niranjan, K.: Long-term variation of OH peak emission altitude and volume emission rate over Indian low latitudes, Journal of Atmospheric and Solar-Terrestrial Physics, 138, 161–168, https://doi.org/10.1016/j.jastp.2016.01.012, 2016.

Smith, A. K.: Global dynamics of the MLT, Surveys in Geophysics, 33, 1177–1230, https://doi.org/10.1007/s10712-012-9196-9, 2012.

Smith, A. K., Harvey, V. L., Mlynczak, M. G., Funke, B., García-Comas, M., Hervig, M., Kaufmann, M., Kyrölä, E., López-Puertas, M., McDade, I., Randall, C. E., Russell III, J. M., Sheese, P. E., Shiotani, M., Skinner, W. R., Suzuki, M., and Walker, K. A.: Satellite observations of ozone in the upper mesosphere, Journal of Geophysical Research: Atmospheres, 118, 5803–5821, https://doi.org/10.1002/jgrd.50445, 2013.

Snively, J.: Mesospheric hydroxyl airglow signatures of acoustic and gravity waves generated by transient tropospheric forcing, Geophysical Research Letters, 40, 4533–4537, https://doi.org/10.1002/grl.50886, 2013.

Tang, J., Kamalabadi, F., Vadas, S. L., and Miller, S. D.: Gravity wave characteristics in the mesopause region revealed from OH airglow imager observations over Northern Colorado, Journal of Geophysical Research: Space Physics, 119, 630–645, https://doi.org/10.1002/2013JA019445, 2014.

Tarasick, D. W. and Shepherd, G. G.: Effects of gravity waves on complex airglow chemistries: 2. OH emission, Journal of Geophysical Research: Space Physics, 97, 3195–3208, https://doi.org/10.1029/91JA02580, 1992.

Taylor, M. J., Pautet, P.-D., Medeiros, A. F., Buriti, R., Fechine, J., Fritts, D. C., Vadas, S. L., Takahashi, H., and São Sabbas, F. T.: Characteristics of mesospheric gravity waves near the magnetic equator, Brazil, during the SpreadFEx campaign, Annales Geophysicae, 27, 461–472, https://doi.org/10.5194/angeo-27-461-2009, 2009.

https://doi.org/10.5194/egusphere-2026-1038
Preprint. Discussion started: 9 March 2026
© Author(s) 2026. CC BY 4.0 License.

Vargas, F., Swenson, G., Liu, A., and Gobbi, D.: O(^{1}S), OH, and O2(b) airglow layer perturbations due to AGWs and their implied effects on the atmosphere, Journal of Geophysical Research: Atmospheres, 112, D14 102, https://doi.org/10.1029/2006JD007642, 2007.

Walterscheid, R. L., Schubert, G., and Straus, J. M.: A dynamical-chemical model of wave-driven fluctuations in the OH nightglow, Journal of Geophysical Research: Space Physics, 92, 1241–1254, https://doi.org/10.1029/JA092iA02p01241, 1987.

765 Weatherhead, E. C., Reinsel, G. C., Tiao, G. C., Meng, X.-L., Choi, D., Cheang, W.-K., Keller, T., DeLuisi, J., Wuebbles, D. J., Kerr, J. B., Miller, A. J., Oltmans, S. J., and Frederick, J. E.: Factors affecting the detection of trends: Statistical considerations and applications to environmental data, Journal of Geophysical Research: Atmospheres, 103, 17 149–17 161, https://doi.org/10.1029/98JD00995, 1998.

Wolter, K. and Timlin, M. S.: Measuring the strength of ENSO events: How does 1997/98 rank?, Weather, 53, 315–324, https://doi.org/10.1002/j.1477-8696.1998.tb06408.x, 1998.

770 Xu, J., Smith, A. K., Mlynczak, M. G., and Russell III, J. M.: Using TIMED/SABER nightglow observations to investigate hydroxyl emission mechanisms in the mesopause region, Journal of Geophysical Research: Atmospheres, 117, D02 301, https://doi.org/10.1029/2011JD016342, 2012.

Yuan, T., Solomon, S. C., She, C.-Y., Krueger, D. A., and Liu, H.-L.: The long-term trends of nocturnal mesopause temperature and altitude revealed by Na lidar observations between 1990 and 2018 at midlatitude, Journal of Geophysical Research: Atmospheres, 124, 5970–5980,

775 https://doi.org/10.1029/2018JD029828, 2019.

Yue, J., Russell III, J. M., Jian, Y., Rezac, L., Garcia, R., López-Puertas, M., and Mlynczak, M. G.: Increasing carbon dioxide concentration in the upper atmosphere observed by SABER, Geophysical Research Letters, 42, 8406–8414, https://doi.org/10.1002/2015GL064696, 2015.

Yue, J., Russell III, J., Jian, Y., Rezac, L., Garcia, R., López-Puertas, M., and Mlynczak, M. G.: Increasing carbon dioxide concentration in

780 the upper atmosphere observed by SABER, Geophysical Research Letters, 46, 11,180–11,188, https://doi.org/10.1029/2019GL084018, 2019.

Zhang, X., Forbes, J. M., Hagan, M. E., Russell III, J. M., and Mlynczak, M. G.: A global morphology of gravity wave activity in the stratosphere revealed by the 8-year SABER/TIMED data, Journal of Geophysical Research: Atmospheres, 117, D21 101, https://doi.org/10.1029/2012JD017676, 2012.

785 Zhao, X., Russell III, J. M., Mlynczak, M. G., Siskind, D. E., Marshall, B. T., Hervig, M. E., and Gordley, L. L.: Long-term trends and solar responses of the mesopause temperatures observed by SABER during the 2002–2019 period, Journal of Geophysical Research: Atmospheres, 125, e2019JD031 759, https://doi.org/10.1029/2020JD032418, 2020.